Baroclinic instability in the West Spitsbergen Current

S. H. Teigen,[1] F. Nilsen,[1,2] R. Skogseth,[1] B. Gjevik,[3] and A. Beszczynska-Möller[4]

Received 24 January 2011; revised 18 March 2011; accepted 7 April 2011; published 15 July 2011.

[1] Baroclinic instability in the West Spitsbergen Current is investigated, based on data from an array of current meter moorings along 78.83°N, across the deeper (1000–2400 m) section of the continental slope west of Svalbard. Numerical linear stability analyses of the current are presented, utilizing a normal mode two-layer linear model and idealizations of the baroclinic velocity field and the cross-shelf bathymetry. The characteristic period, wavelength, and growth rate of unstable vorticity waves are revealed, appearing as two distinct peaks in growth rate, with typical wave periods of 35–75 h and wavelengths 15–30 km. The resulting vorticity wave structure of the dominant unstable mode is centered close to the position of the maximum current. Wavelet and rotary spectrum analysis of the current meter data from September 2007 to July 2009 detect transient signals with significant energy at similar oscillation periods as indicated by the linear stability analysis, which suggests that the baroclinic instability process is active during ~30% of the measurement record and is most pronounced during winter/spring. Unstable vorticity waves represent an effective mechanism for cooling the core of the West Spitsbergen Current by isopycnal transport of water masses from the core to the surface. The heat loss associated with the most unstable mode is estimated to reach 240 W m^{-2}, which is comparable with reported values of winter surface heat loss.

Citation: Teigen, S. H., F. Nilsen, R. Skogseth, B. Gjevik, and A. Beszczynska-Möller (2011), Baroclinic instability in the West Spitsbergen Current, *J. Geophys. Res.*, *116*, C07012, doi:10.1029/2011JC006974.

1. Introduction

[2] The West Spitsbergen Current (WSC) brings warm and saline Atlantic water masses into the Polar Basin, and constitutes the main source of oceanic heat and salt to the Arctic Ocean [*Aagaard and Greisman*, 1975]. The current consists of an eastern and a western branch (see the embedded map in Figure 1). The western branch originates in the offshore branch of the Norwegian Atlantic Current, which travels along the fracture zones in the Norwegian Sea as a baroclinic frontal jet [*Orvik and Niiler*, 2002; *Walczowski and Piechura*, 2007]. The eastern branch of the WSC slope current consists of a slope/break confined barotropic component occupying the upper 750 m of the water column between the 1000 m isobath and the West Spitsbergen shelf break, and a more baroclinic component over the deeper slope between the 1000 m and 2400 m isobaths [*Gascard et al.*, 1995; *Schauer et al.*, 2004]. North of 79°N, the eastern WSC branch separates into the Svalbard branch and the Yermak branch [*Gascard et al.*, 1995]. The Svalbard branch passes over the Yermak plateau (600 m deep) and continues into the Arctic Ocean along the continental slope of the Eurasian Basin [*Dmitrenko et al.*, 2008]. The Yermak branch mainly originates in the baroclinic eastern branch of the WSC (termed the "1500 m WSC branch" by *Gascard et al.* [1995]), travels around the Yermak Plateau and mixes [*Sirevaag and Fer*, 2009; *Fer et al.*, 2010] with ambient water masses along its path. Recirculating branches shoot off from the western WSC branch, flowing along the topographic fracture zones (FZ) in the Fram Strait (the Molloy, Hovgaard and Spitsbergen fracture zones). The recirculating branches are mainly composed by eddies [*Gascard et al.*, 1995], adding heat and salt to the Greenland Sea. According to *Manley* [1995], around 55% of the Atlantic Water transported by the WSC enters the Arctic Ocean (30% in the Svalbard Branch and 25% in the Yermak branch), while the remaining 45% recirculates in the Fram Strait. Based on summer CTD and ADCP transects across the WSC, *Walczowski et al.* [2005] documented the multipath structure and strong barotropic component of the current. They found that AW transport estimates generally became 2–3 times higher when based on direct current measurements rather than traditional geostrophic calculations.

[3] Upstream modification of the Atlantic water masses influences the strength and geographical localization of the deep convection in the Greenland Sea [*Saloranta and Haugan*, 2001] and the properties of both the source water of overflow from the Nordic Seas [*Eldevik et al.*, 2009] and the Atlantic layer of the Arctic Ocean [*Steele and Morison*, 1993; *Steele and Boyd*, 1998]. On its way to the Arctic Ocean, the subsurface core of the eastern barotropic West Spitsbergen

[1]Department of Arctic Geophysics, University Centre in Svalbard, Longyearbyen, Norway.
[2]Geophysical Institute, University of Bergen, Bergen, Norway.
[3]Department of Mathematics, University of Oslo, Oslo, Norway.
[4]Alfred Wegener Institute for Polar and Marine Research, Bremerhaven, Germany.

0148-0227/11/2011JC006974

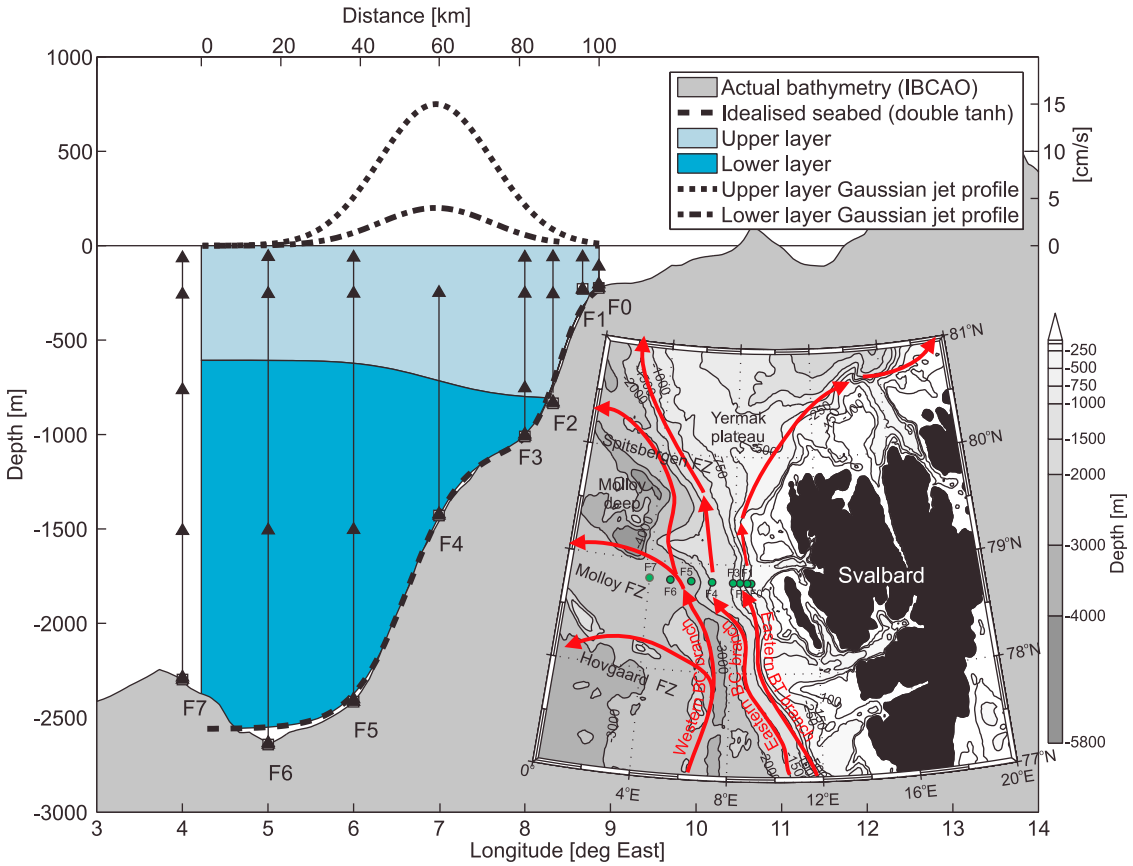

Figure 1. Actual bathymetry (gray) along the mooring section and idealized shelf profile $h(x)$. Moorings and current meter positions are marked with vertical lines and solid triangles, respectively. Illustrating examples of the modeled Gaussian current profiles in the two layers and the layer interface are also shown. The geographical positions of the current meter moorings are shown on the map to the right. Bathymetry is based on the International Bathymetric Chart of the Arctic Ocean [*Jakobsson et al.*, 2008]. The main circulation branches of the West Spitsbergen Current are indicated with red arrows.

Current branch is rapidly cooling, up to −0.31°C 100 km^{-1} during wintertime [*Saloranta and Haugan*, 2004]. This cooling is decisive for the vertical depth of the Atlantic input to the Arctic Ocean. An increased upward oceanic heat flux from the intruding Atlantic water in the Arctic Ocean could lead to a rapid loss of the remaining sea ice cover [*Turner*, 2010].

[4] *Helland-Hansen and Nansen* [1912] commented on undulations in the isotherms and isohalines of hydrographic sections across the WSC, attributing them to periodical movements of the water masses. Eddy fields generated by baroclinic and barotropic instability [*Teigen et al.*, 2010] represent a vital mechanism for advecting water isopycnally from the warm core to the surface, thereby cooling the WSC [*Boyd and D'Asaro*, 1994; *Nilsen et al.*, 2006]. Using a quasi-geostrophic two-layer model with uniformly sloping topography and uniform currents in each layer, *Mysak and Schott* [1977] found that the oscillation period of modeled unstable baroclinic shelf waves matched periodic signals in a time series from the Norwegian Atlantic Current at 63°N. *Hanzlick* [1983] utilized the same model with parameters representative of the WSC and the West Spitsbergen Slope (WSSl), finding wave periods of 3–4 days, with wavelengths 30–40 km. The western branch of the WSC shows more variable and eddying character and is assumed to be mainly recirculating in or near the Fram Strait and joining the EGC [*Bourke and Paquette*, 1988; *Gascard et al.*, 1995]. *Gascard et al.* [1988] hypothesized that eddies may explain a significant part of the east-west recirculation pattern in the Fram Strait. Drifter trajectories obtained during the Marginal Ice Zone Experiment (MIZEX) [*Johannessen et al.*, 1987] showed that eddies were almost permanently generated along the entire WSSl, with an approximate horizontal size of 20–30 km and a rotational period of 6–7 days. After separation from the main current, the path of the eddies seemed to be controlled by topography.

[5] *Nilsen et al.* [2006] estimated the lateral heat flux due to stable topographic waves along the West Spitsbergen Shelf (WSS), while *Teigen et al.* [2010] considered the heat exchange associated with unstable barotropic modes near the shelf break. In the present study, we focus on the baroclinic eastern WSC branch, modeling the observed situation of Atlantic Water (AW, defined by *Aagaard et al.* [1985] as water with temperature $T > 2$°C and salinity $S > 34.9$ PSU) residing over colder Lower Arctic Intermediate Water (LAIW, defined by *Aagaard et al.* [1985] as water with $T < 2$°C, $S > 34.9$ PSU) in the Fram Strait by utilizing a two-layer model. Inspired by the suggestions of *Mysak and Schott* [1977], that

Table 1. Overview (Position, Depth, Deployment/Retrieval Data) of Moorings F5–F3 Over the Deep Section of the West Spitsbergen Slope[a]

	Mooring		
	F5	F4	F3
Latitude	78°50′N	78°50′N	78°50′N
Longitude	6°00′E	7°00′E	8°00′E
Model position (km)	40	59	81
Water depth (m)	2415	1429	1010
Deployment date	12 Sep 2007	12 Sep 2007	28 Sep 2007
Retrieval/redeployment date	5/12 Jul 2008	5/7 Jul 2008	5/7 Jul 2008
Retrieval date	3 Jul 2009	3 Jul 2009	3 Jul 2008

[a]The corresponding grid positions used in the linear stability model are also given.

the effect of lateral shear and more complex topography should be investigated in the context of baroclinic instability, we employ a linear analysis that allows for zonal shear and a topography with variable slope. In section 2, the data is presented along with the theory behind the linear two-layer stability analysis. The results from the linear stability analysis and the data analysis are presented in section 3. In section 4, the properties of the unstable baroclinic vorticity waves and the associated heat fluxes in the WSC are discussed. The main conclusions of the paper are summarized in section 5.

2. Data and Methods

2.1. Current Meter Data

[6] The analysis is based on data from an array of current meter moorings across the eastern Fram Strait [*Schauer et al.*, 2004, 2008], where the focus is on the three moorings (F3, F4 and F5) covering the WSSl region between 1000 and 2400 m depth. The positions are shown in Figure 1. Details of the moorings are summarized in Table 1. The mooring section has been maintained by the Alfred Wegener Institute since 1997 as part of the European Union projects VEINS (1997–2000), ASOF-N (2002–2005) and EU-DAMOCLES (2006–). The analysis is based on data from the deployments between September 2007 and July 2009, which covers the period (September 2007 to July 2008) studied by *Teigen et al.* [2010].

[7] In Figure 2, progressive vector diagrams of the current at the 250 m and 1500 m depth levels at mooring F4 are shown. The orientation of the current is relatively stable, although the current at the 250 m level displays flow reversal events in April–September 2008 and February–March 2009. There are several episodes of intense flow maxima at the 250 m level during winter (as can be seen by the longer separation between date labels), a feature also remarked in other studies [*Morison*, 1991; *Fahrbach et al.*, 2003; *Schauer et al.*, 2004]. The magnitude of the flow at the 1500 m level is more steady throughout the year. The temperature at the 250 m level is going through a seasonal cycle, with a maximum temperature of 4.0–4.5°C in November–December and a minimum around 2.5°C in May. Isolated episodes of colder intrusions happen throughout the winter, with temperatures below 2.0°C. The deepest instrument is situated inside the LAIW in the Fram Strait/Greenland Sea and has a steady temperature of around −0.88°C.

2.2. Two-Layer Model

[8] In a former study by *Gjevik* [2002], the matrix equation for the normal modes of a two-layer shallow water system

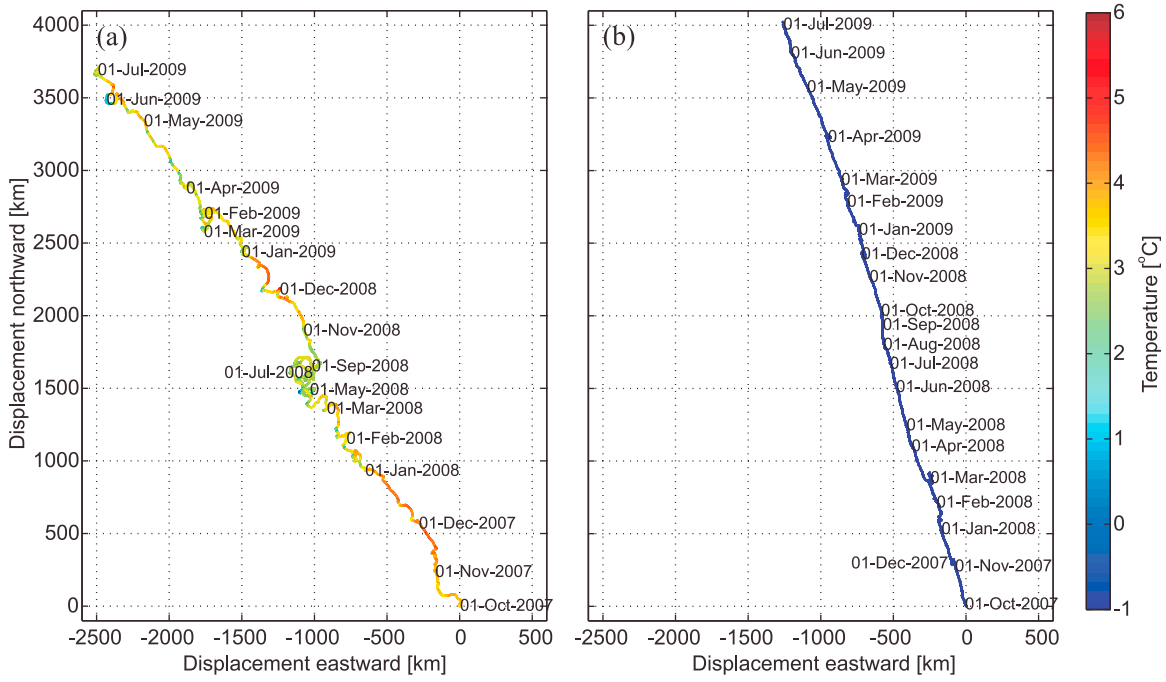

Figure 2. Progressive vector diagrams of the current at mooring F4 in (a) the 250 m level and (b) the 1500 m level. The associated temperature record is plotted in color. For better readability, only every second month is labeled between 1 March 2008 and 1 November 2008 in Figure 2a.

(see Figure 1) with no background flow in the lower layer was derived. *Teigen* [2011] expanded the model to allow for a flow in the lower layer as well. Below, the model is briefly presented, for more details, see *Teigen* [2011]. Subindices 1 and 2 refer to variables in the upper layer and lower layer, respectively. The u component is pointing east toward the shore, while the v component is in the along-shelf direction (pointing north along isobaths).

[9] We assume a steady, along-slope, geostrophically balanced background current on a f plane. Upon integration this yields for the displacement of the surface $\overline{\eta}_1$

$$\overline{\eta}_1 = -\frac{f}{g}\int_x^{L_x} \overline{v}_1 \mathrm{d}x, \tag{1}$$

where $f = 1.42 \times 10^{-4}$ [1 s^{-1}] is the Coriolis parameter, $g = 9.81$ m s^{-2} is the acceleration of gravity, L_x is the total width of the channel and $\overline{v}_1$ is the steady along-slope background current in the upper layer. For the displacement of the interface between the two layers, $\overline{\eta}_2$, we have

$$\overline{\eta}_2 = -\frac{f}{g'}\int_x^{L_x} \overline{v}_2 \mathrm{d}x - \frac{g\overline{\eta}_1}{g'}, \tag{2}$$

where $\overline{v}_2$ is the background current in the lower layer and $g' = g\frac{\rho_2-\rho_1}{\rho_2}$ [m s^{-2}] is reduced gravity; ρ_1 and ρ_2 are the densities in the upper and lower layers, respectively.

[10] We introduce small perturbations to the background flow, according to

$$\eta_n = \overline{\eta}_n + \eta_n', \tag{3a}$$

$$u_n = u_n', \tag{3b}$$

$$v_n = \overline{v}_n + v_n'. \tag{3c}$$

In equations (3a)–(3c), primed quantities are perturbations. Subscript n refers to layer n = 1, 2. We search for normal modes on the form

$$\eta_n' = \hat{\eta}_n(x)\cos(ky - \omega t), \tag{4a}$$

$$u_n' = \hat{u}_n(x)\sin(ky - \omega t), \tag{4b}$$

$$v_n' = \hat{v}_n(x)\cos(ky - \omega t), \tag{4c}$$

where k is wave number, t is time, $\omega = \omega_r + \mathrm{i}\omega_i$ is complex angular velocity and the complex phase speed is $c = c_r + \mathrm{i}c_i = \frac{\omega}{k}$. Inserting the normal modes into the linearized version of the two-layer shallow water equations, leads to a matrix equation for the complex frequency ω, which can be solved by numerical eigenvalue methods. For $\omega_i > 0$, the wave solution is unstable and the amplitude of the perturbations will grow exponentially with growth rate $\gamma = \omega_i = kc_i$ and wave period $P = 2\pi/\omega_r$.

[11] The modeled WSS topography is uniform in the along-shelf direction, and the undisturbed water depth, $h(x)$, is represented by a smooth double tanh function in the across-shelf direction resolving the two-step nature of the slope (see Figure 1)

$$h(x) = a_1\left(1 - g_1\tanh\left(\frac{x-x_1}{s_1}\right)\right) + a_2\left(1 - g_2\tanh\left(\frac{x-x_2}{s_2}\right)\right) - a_2(1-g_2), \tag{5}$$

where $a_1 = 621$ m, $g_1 = 0.7069$, $x_1 = 90$ km, $s_1 = 7$ km, $a_2 = 2350$ m, $g_2 = 0.3191$, $x_2 = 52$ km and $s_2 = 14$ km. The same bathymetric profile was used by *Nilsen et al.* [2006] and *Teigen et al.* [2010]. The maximum upper bottom slope is $\sim 6 \times 10^{-2}$ and somewhat steeper than the maximum deep bottom slope ($\sim 5 \times 10^{-2}$). The more gently sloping segment between the two slopes is $\sim 1 \times 10^{-2}$. For the WSS configuration, the density interface between the two layers intersects the bottom topography (Figure 1), resulting in an offshore two-layer region and an onshore monolayer region [*Kawabe*, 1982].

[12] The background current field in both layers is modeled as a Gaussian jet, given by

$$\overline{v}_n(x) = \overline{v}_{0,n}\exp\left[-\left(\frac{x-L_B}{B}\right)^2\right], n = 1, 2. \tag{6}$$

Here, L_B is the position of the current maximum, while $\overline{v}_{0,n}$ is the maximum current speed in layer n and B is the half width of the jet. L_B and B are assumed to be the same in the two layers.

[13] The width of the calculation domain is $L_x = 100$ km. The lateral boundary condition at $x = 0$ and $x = L_x$ is zero normal velocity, i.e., $u_n' = 0$. A grid size of $\Delta x = 0.5$ km proved to be sufficient for numerical convergence, provided that the current profile has a smooth derivative. Calculations were made for wavelengths in the range 10 to 100 km, with intervals of 0.5 km. For plotting of the modal structures, the eigenvectors were scaled in the same manner as done by *Teigen et al.* [2010].

[14] *Mysak and Schott* [1977] described an analytical model for calculation of the unstable baroclinic modes of a shelf current in a two-layer system with step-wise uniform current in the two layers, providing a suitable test case for the present numerical model. In Figure 3, the dispersion relation calculated with the parameter choices given by *Mysak and Schott* [1977] for the Norwegian Atlantic Current at 63°N is shown for two different values of reduced gravity. The similarities between the results obtained with the present model and that of *Mysak and Schott* [1977] are evident, although the growth rate is slightly higher for their model (8% in Figure 3a and 5% in Figure 3b). The wave period also differs 5–10% for the long periodic bands of stable modes when $g' = 0.5 \times 10^{-2}$ m s^{-2} (Figure 3a). The present model retains a free surface and the fact that the difference is larger for weaker stratification indicates that the rigid lid boundary condition assumed by *Mysak and Schott* [1977] may be a plausible explanation for the deviation. Tests with refined horizontal grid size show that the grid resolution cannot be the cause of the deviation [*Teigen*, 2011]. The lowest stable mode in the present model is the internal gravity wave, and corresponds well with the analytical curve (Figures 3a and 3b).

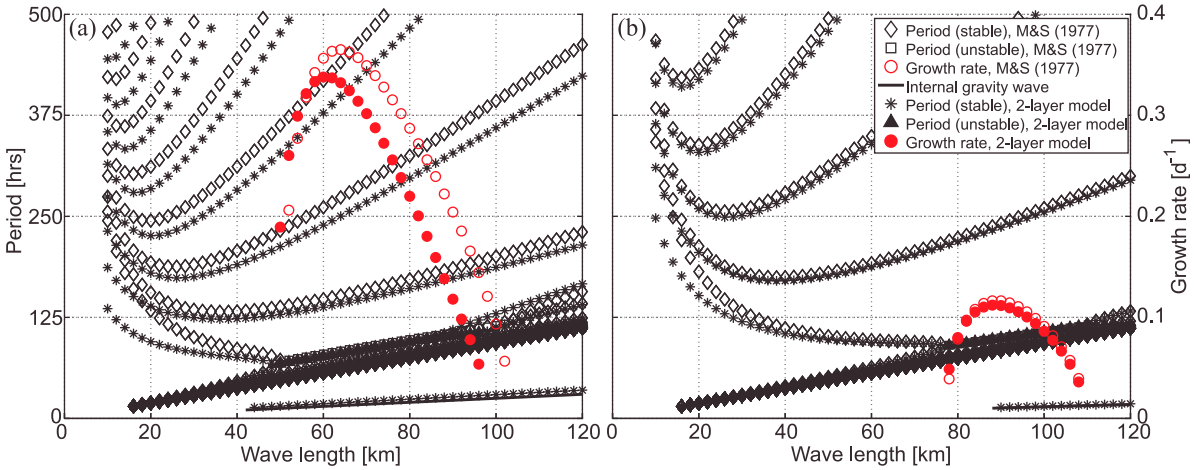

Figure 3. Comparison of the dispersion relation calculated with the model by *Mysak and Schott* [1977] and the present model: (a) $g' = 0.5 \times 10^{-2}$ m s^{-2} and (b) $g' = 1.5 \times 10^{-2}$ m s^{-2}. The analytical dispersion relation of the internal gravity wave (flat bottom) is also shown.

[15] From standard linear stability theory of quasi-geostrophic flows [*Pedlosky*, 1964; *Mysak et al.*, 1981a] a condition for exponential growth ($c_i > 0$) of a two-layer system with no horizontal shear ($\bar{v}_1$, $\bar{v}_2$ constant) and uniformly sloping topography can be derived as

$$\frac{\bar{v}_1 - \bar{v}_2}{|\bar{v}_1 - c|^2}\int_0^{L_x} |\Phi_1|^2 dx - \frac{\bar{v}_1 - \bar{v}_2}{|\bar{v}_2 - c|^2}\int_0^{L_x} |\Phi_2|^2 dx - \frac{g'\alpha/f}{|\bar{v}_2 - c|^2}\int_0^{L_x} \cdot |\Phi_2|^2 dx = 0. \quad (7)$$

Here Φ_n, $n = 1, 2$ is the complex amplitude in layer n of a normal mode unstable solution to the linearized quasi-geostrophic potential vorticity equation and α is the topographical slope. From this condition it can be seen that the possibility of an unstable solution is closely related to strong shears, e.g., for $\bar{v}_1 - \bar{v}_2$ large and positive, the two first terms could strike a balance, which is needed if an unstable solution should exist. For strong slopes ($|\alpha|$ large) and/or strong stratification (g' large), the third term would dominate the others, rendering instability unlikely. However, if $\bar{v}_1 \approx c$ (for $\bar{v}_1 > \bar{v}_2$) or $\bar{v}_2 \approx c$ (for $\bar{v}_2 > \bar{v}_1$), the first or the second term will become large and could cancel the third term.

2.3. Construction of Input to the Linear Stability Analysis

[16] A time series of reduced gravity g' is calculated from the difference between the density measured at the 250 m depth level and the mean density from the 1000 m depth level at F3 (the instrument at the 1000 m level malfunctioned in the 2008–2009 deployment year). The thickness d of the upper layer at F3 is estimated by assuming a linear slope in density between the two depth levels, and using the 1028 kg m^{-3} isopycnal as proxy for the interface between the two layers. The reason for only using F3 is that this mooring was the only one to have measurements of temperature and salinity inside the core of the Atlantic layer. The 1028 kg m^{-3} isopycnal defines the TS path between LAIW and AW at the mooring position [*Cokelet et al.*, 2008]. In the study by *Teigen et al.* [2010], the velocity profile of the barotropic inner branch (core position between moorings F1 and F2) was constructed by fitting an asymmetric function to the measured velocities. This was possible due to the relatively densely spaced (4–7 km) current meter moorings over the shallower (200–1000 m depth) section of the slope. In the baroclinic eastern branch, the mooring spacing is coarser (20 km) and correlation is poorer between the moorings. Hence, the strategy for constructing the velocity profile had to be simplified. Based on CTD sections across the WSSl, a Gaussian current profile is generally a fair first-order approximation to make the layer interface resemble the shape of the isopycnal between LAIW and AW over the outer slope. The velocity profile is represented by a Gaussian profile (6) in both layers, centered at F4 ($L_B = 59$ km), with half width $B = 20$ km. The maximum current amplitude $\bar{v}_{0,1}$ in the upper layer is given by the 30 day smoothed average along-shelf (the 1500 m isobath at the mooring site is pointing along 335° bearing) current component at the 250 m level, while the maximum amplitude $\bar{v}_{0,2}$ in the lower layer is given by the smoothed along-shelf current component at 1500 m. The interface between the two layers is modified by the background baroclinic velocity field according to equation (2). The resulting time development of the interface between the two layers is illustrated in Figure 4.

3. Results

3.1. Wavelet Analysis

[17] The periodic signal of an unstable baroclinic vorticity wave is expected to be transient. For this reason, wavelet analysis [*Torrence and Compo*, 1998] is utilized, which enables a survey of both the dominating oscillation periods and their variation in time. The Morlet wavelet, described as a plane wave, focused in time by Gaussian damping, was chosen as mother function. For the computations of the wavelet spectrum the toolbox by *Torrence and Compo* [1998] was used. *Liu et al.* [2007] showed that there is a bias toward elevated levels of energy in the long periodic range of the spectrum with this toolbox and proposed a modification to correct for this. The correction has been applied in the present analysis. Figures 5a–5f shows wavelet power spectra of the

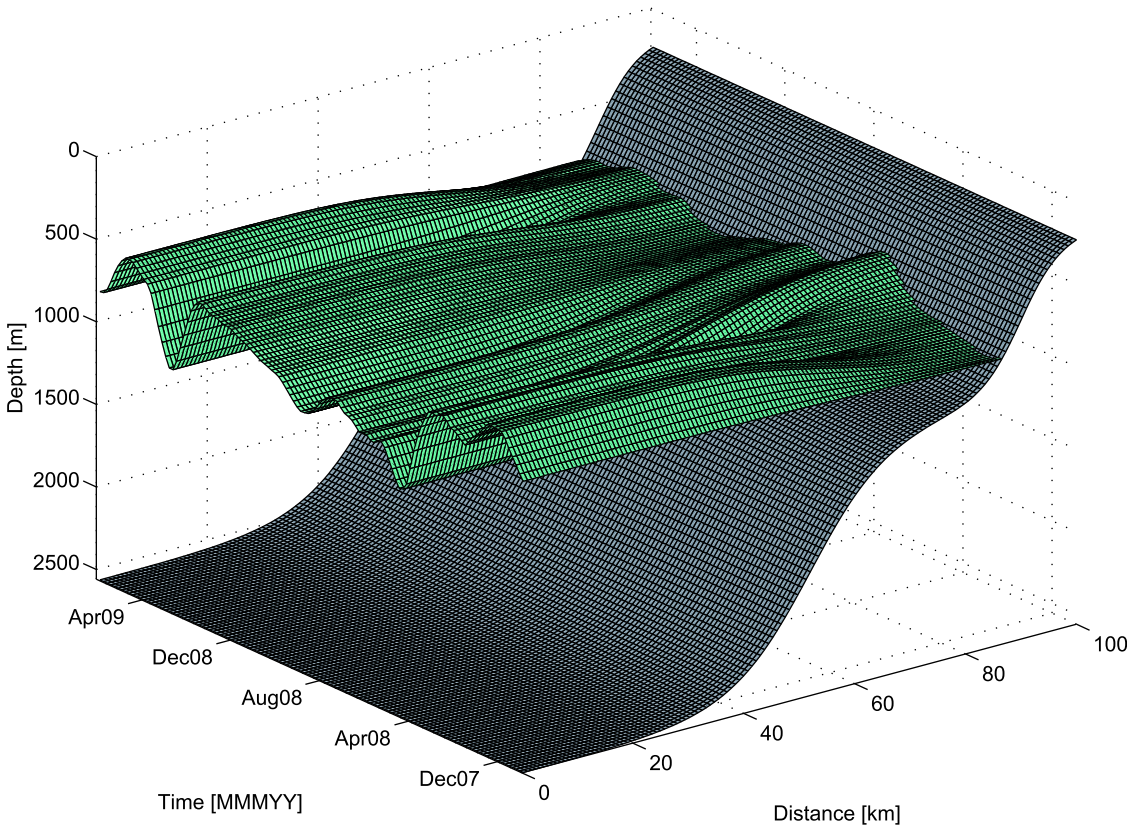

Figure 4. Time evolution of the interface between the two layers (green). The topography is shown in gray.

across-shelf (easterly) current (u), along-shelf (northerly) current (v), and temperature (T) at the 250 m and 1500 m depth levels of mooring F4. Singular episodes of significant wavelet power for long periodic oscillations (with longer period than the diurnal tide K1) are present in all velocity spectra (Figures 5a–5d), mainly focused around the winter and spring months (December–May). We often find the highest energy in this period range as well. The semidiurnal tide M2 is clearly present in the along-shelf current component (Figures 5c and 5d), and the fortnightly period of the neap-spring tide can also be discerned. As noted by *Kasajima and Svendsen* [2002], the along-shelf (or rather northerly) component seems to dominate for the semidiurnal tide. The energy of the diurnal tide K1 is rarely above the confidence level, but has been shown to increase in the upslope direction [*Kasajima and Svendsen*, 2002; *Nilsen et al.*, 2006; *Teigen et al.*, 2010]. The wavelet power spectrum of temperature in the 250 m level (Figure 5e) also undergoes an annual cycle, with frequent episodes of energetic long periodic signals during the winter months, while the summer months are more quiet. For the 1500 m level (Figure 5f), there is no apparent annual cycle in the power spectrum of temperature, the few isolated events of increased power occur during midsummer and midwinter.

3.2. Results From the Linear Stability Analysis

[18] Linear stability analysis determines the initial temporal and spatial scales of the most unstable modes. The structure of these exponentially growing modes is retained even after the system becomes fully nonlinear. This is a common feature for unstable flows and can also be seen from numerical experiments of the evolution of eddies in an unstable shelf edge jet by *Davies et al.* [2003]. The stability analysis was run with input from moorings F4 and F3 (see section 2.3), producing a time series of the characteristics of the dominant unstable baroclinic vorticity wave. The most unstable conditions (highest modeled growth rate) occurred on 28 November 2007. Maximum speed in the upper layer ($\overline{v}_{0,1}$), lower layer ($\overline{v}_{0,2}$), interface depth (d), and reduced gravity (g') were then 0.17 m s^{-1}, 0.04 m s^{-1}, 841 m, and 2.2×10^{-3} m s^{-2}, respectively. In Figure 6, the detailed dispersion relation from the linear stability analysis of these conditions is presented. For phase speeds between the upper and lower layer flow speed, a vast set of stable modes exist. A multitude of discrete bands of unstable modes can also be seen. Compared with the relative simplicity of the dispersion relation depicted in Figures 3a and 3b, the dispersion relation of the WSC configuration shows a rich variety of modes. The increased complexity arises due to the across-shelf variation of both current and topography, allowing the different modes to combine in new ways. However, two bands of unstable modes stand out with higher growth rate and persistence over a broader range of wavelengths than the others. This makes them likely to dominate. The gray regions below $c = \overline{v}_1$ and above $c = \overline{v}_2$ correspond to regions where there is an infinite number of discrete modes [*Mysak et al.*, 1981b]. The mode with the overall highest growth rate appears on the band of unstable modes between 22 and 28 km wavelength (the peak of this band is referred to as the primary unstable mode, and is indicated with a red arrow in

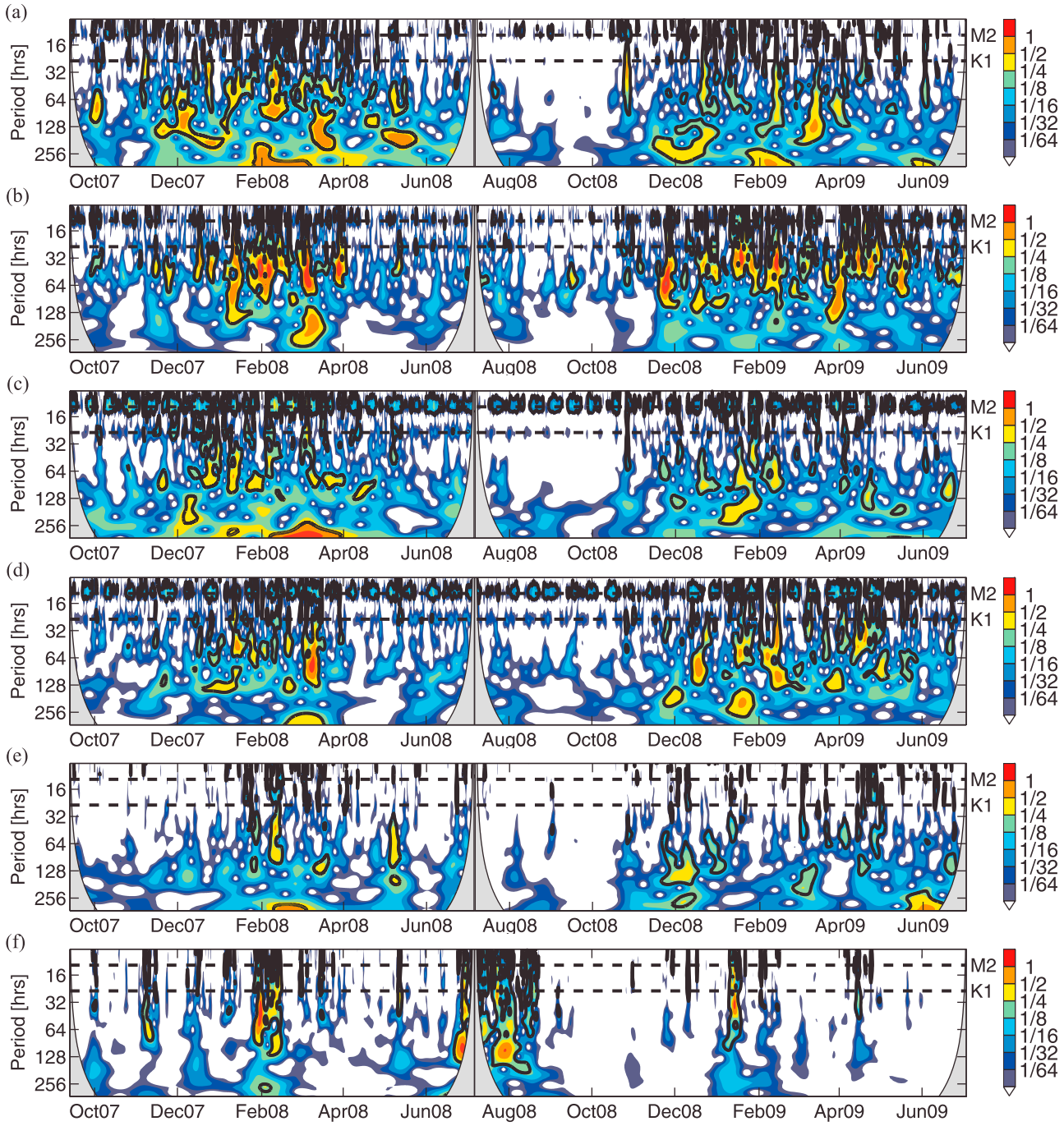

Figure 5. Wavelet power spectra of (a) u at the 250 m depth level, (b) u at the 1500 m depth level, (c) v at the 250 m depth level, (d) v at the 1500 m depth level, (e) T at the 250 m depth level, and (f) T at the 1500 m depth level from mooring F4, throughout the deployment period from September 2007 to July 2009. The power is normalized by the variance $1/\sigma^2$. The periods of M2 (12.42 h) and K1 (23.93 h) are indicated by dashed lines. Regions with power above the 95% confidence level are enclosed by black contours.

Figure 6), at a phase speed of 0.136 m s^{-1}. The primary peak in growth rate is γ = 0.073 day^{-1}. The corresponding wavelength is ~25.5 km and the associated wave period is ~53 h for the primary mode. The second strongest band of unstable modes extends from 27 to 36 km (the peak of this band is referred to as the secondary unstable mode, and is indicated with a green arrow in Figure 6), slightly overlapping in wavelength with the primary mode. The secondary peak in growth rate is γ = 0.034 day^{-1} and occurs at a phase speed of 0.125 m s^{-1}. The corresponding wavelength is ~31 km and the associated wave period is ~70 h. In Figure 7a, the modal structure associated with the primary

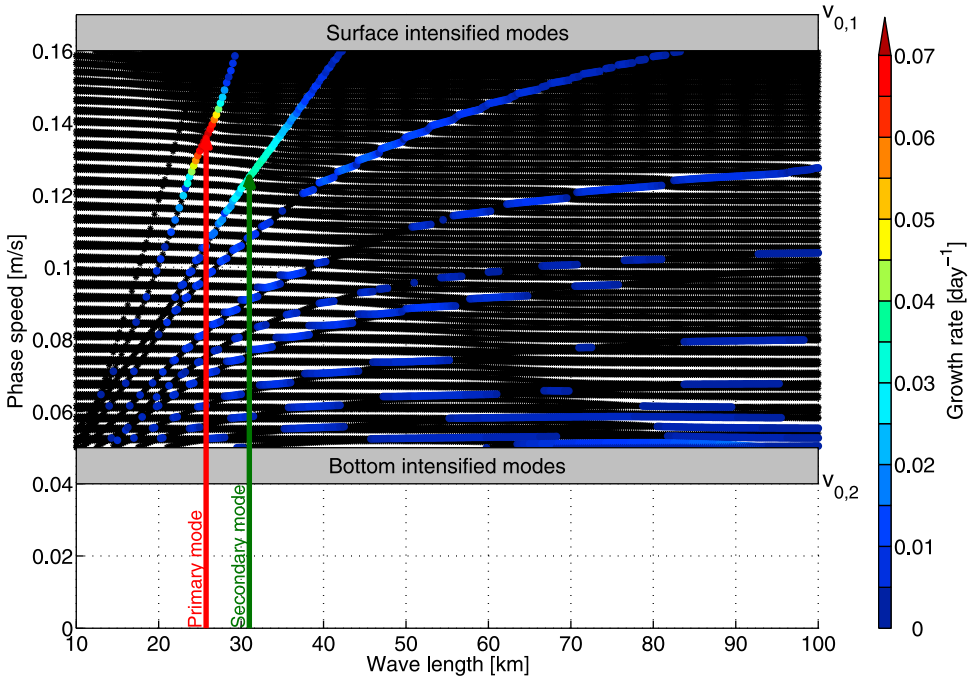

Figure 6. Dispersion diagram obtained by linear stability analysis of the conditions that resulted in the highest growth rate (28 November 2007). The phase speed of stable (black dots) and unstable modes (colored circles) are shown. The color scale of the unstable modes is given by the growth rate. The primary and secondary peaks in growth rate are indicated with red and green arrows, respectively.

unstable mode is shown for the upper layer. The center of the vorticity wave is located close to F4, the position of the maximum vertical current shear. In Figure 7b, the modal structure associated with the primary unstable mode is shown for the lower layer. The upper layer lags the lower layer by a phase angle of 56°. The center of the vorticity wave is positioned a few kilometers offshore of F4, and the vorticity structure extends all the way to the intersection between the layer interface and the continental slope. The cross-shelf extension of the wave is ~20 km in the upper layer and ~40 km in the lower layer. In Figures 7c and 7d, the modal structures of the secondary unstable mode are shown for the upper (Figure 7c) and lower (Figure 7d) layers. A dipole structure can be seen, with vorticity centers both east and west of F4. The easterly vorticity center dominates in the upper layer, while in the lower layer they are more similar in strength. In the lower layer, the wave structure is cell like and the oscillation is intensified at the intersection between the layer interface and the shelf slope. The upper layer lags the lower layer by a phase angle of 46°.

[19] The detailed time series of the fitted baroclinic jet parameters (maximum current amplitude in the two layers, interface depth and reduced gravity) are plotted in Figures 8a and 8b. Assuming that the unstable mode with the highest growth rate is most likely to dominate, and hence show up in the observations, the time evolution in wavelength, wave period, and growth rate of the primary mode are displayed for the entire measurement record in Figures 8c–8e. For completeness, the secondary mode is also shown. Unstable conditions with a growth rate >0.005 day^{-1} are encountered during ~30% of the time record. For the first and most significant episode of baroclinic instability (mid-November 2007 to early January 2008), the mean wavelength of the primary unstable mode was 22 km, mean period was 50 h and mean growth rate was 0.034 day^{-1}. The mean wavelength of the fastest growing mode is ~2.5 times the mean internal Rossby radius of deformation ($r_i = \frac{\sqrt{g'd}}{f}$), confirming that the instability occurs on a scale on the order of (or exceeding) the deformation radius, a requirement for self amplification [*Cushman-Roisin and Beckers*, 2011]. During the same episode, the mean wavelength of the secondary unstable mode was 27 km, mean period was 64 h and mean growth rate was 0.017 day^{-1}. The scale-averaged wavelet spectrum [*Torrence and Compo*, 1998] of u and v was calculated for a ±10% band around the wave period of the primary unstable mode, for the current meters at the 250 m and 1500 m levels. The resulting power is compared with the 95% confidence level corresponding to a red noise background process. Figure 8f indicates the time intervals when the oscillation periods of the primary and secondary unstable modes step out with significant power in the scale-averaged wavelet spectra of u and v at the two current meters. For all the unstable episodes there are time intervals of significant wavelet power at the same oscillation period as predicted by the model

3.3. Sensitivity Study of the Linear Stability Analysis

[20] Figure 9a shows the results from a sensitivity study, varying the shear Rossby number ($Ro = (\bar{v}_{0,1} - \bar{v}_{0,2})/fB$, represented by the maximum speed of the current in the upper layer) and Burger number ($Bu = g'd/f^2B^2$, represented by reduced gravity) systematically. The half width, B, upper layer thickness, d, and the amplitude of the lower layer speed, $\bar{v}_{0,2}$, were kept constant at 20 km, 800 m, and 0.05 m s^{-1}, respectively. The Burger number determines the relative importance between rotation and stratification effects. The

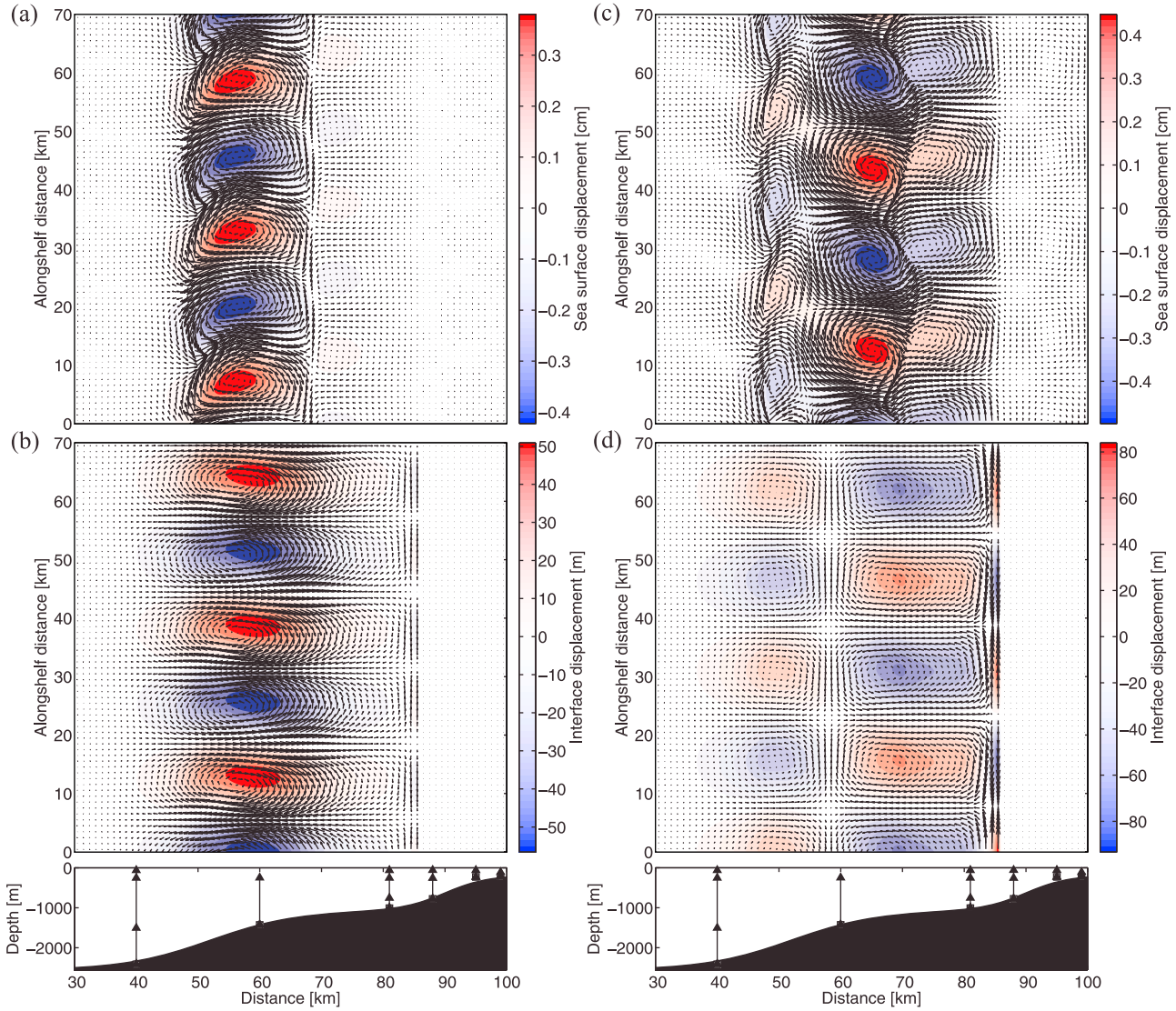

Figure 7. The perturbation modal structure (black vector arrows) and displacement field (red/blue) associated with the primary and secondary unstable mode for the conditions on 28 November 2007: (a) upper and (b) lower layer structure of primary unstable mode and (c) upper and (d) lower layer structure of secondary unstable mode.

growth rate increases with decreasing values of the Burger number and increasing values of the Rossby number. The fact that stronger stratification inhibits instability is to be expected from the condition for baroclinic instability (7). The last term in (7) would dominate for high values of g', displacing the balance which is required for a nonzero growth rate. An increase in Rossby number also leads to longer wavelengths. For strong stratification, an increase in *Ro* also leads to shorter wave periods, while for weaker stratification, *Ro* has less impact on the wave period. Variations in the Burger number do not seem to have a huge influence on the wavelength, but stronger stratification yields longer wave periods. One interpretation of the Burger number is that it compares the ratio between kinetic energy and available potential energy [*Cushman-Roisin and Beckers*, 2011]. The fact that the highest growth rates are confined to small Burger numbers reflects that the bulk of the energy in the background flow must be in the form of available potential energy, which the baroclinic instability can feed on. In order to investigate the influence of the parameters that are kept constant in the analysis in section 3.2 (half width, B, and jet position, L_B) a sensitivity analysis of these parameters was carried out (Figure 9b). Here, d, $\overline{v}_{0,1}$, and $\overline{v}_{0,2}$ were kept constant at 800 m, 0.2 m s^{-1}, and 0.05 m s^{-1}, respectively. It becomes clear that in the vicinity of the chosen values for B and L_B (20 and 59 km, respectively), the resulting values of wavelength, period and growth rate are not very sensitive to changes ±5 km in either B or L_B. There is a local maximum in growth rate around the position of F4. Further inshore or offshore, the growth rate is decreasing, except for narrow half widths, which may lead to horizontal shear instability. If the maximum current moves out to the deep ocean (at F5 and further offshore), the secondary unstable mode becomes the dominant one, switching to longer wavelengths and periods. The overall growth rate is also decreasing as the current maximum moves offshore. About 10 km inshore of F4, there

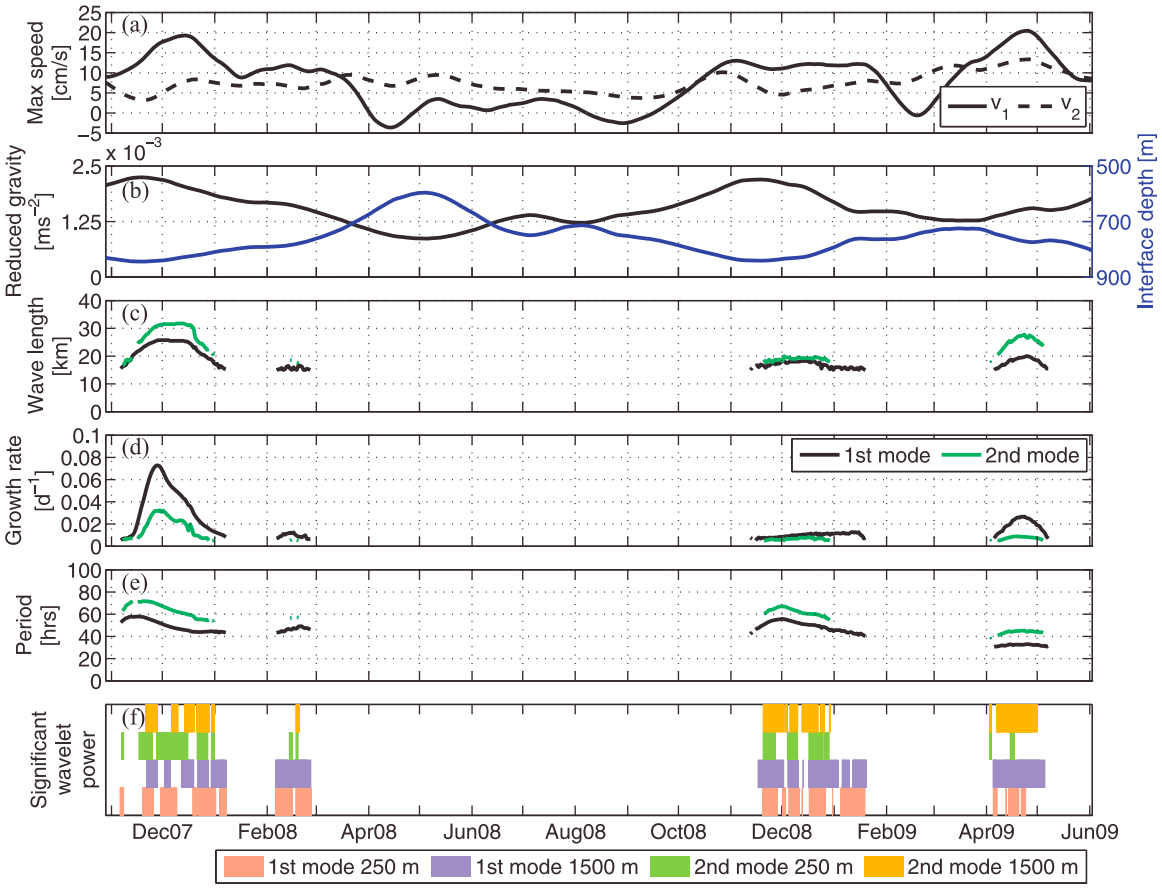

Figure 8. Time series of unstable events: (a) the maximum speed of the fitted current profile, (b) reduced gravity and interface depth of the two-layer model, (c) the wavelength, (d) growth rate and (e) period of the gravest primary (black) and secondary (green) unstable modes, and (f) intervals where the period of the primary or secondary unstable modes matches a period with significant wavelet power in u or v in either the upper layer (250 m) or the lower layer (1500 m) are indicated with colored regions.

is a domain with increasing growth rates, due to the thinning of the lower layer. A current maximum at this location would resemble the barotropic WSC branch over the upper slope, which is treated by *Teigen et al.* [2010].

3.4. Spatial Coherence and Complex Demodulation

[21] Inner and outer rotary coherence spectra [*Livingstone and Royer*, 1980] for the current time series are calculated in order to study rotating current vectors. The inner spectral functions describe corotating components and outer functions describe counterrotating components. The same applies to the rotating phase spectra. Figure 10 shows the outer (Figure 10a) and inner (Figure 10b) coherence spectrum between current meters from the 2008–2009 time series at F4 and F5 at 250 m depth. Based on the time series of unstable events (Figure 8e), we focus on rotational cyclonic and anticyclonic components for periods around 50 h and 70 h. These are period band centers of the primary and secondary unstable modes determined by the analysis in section 3.2. As shown in Figures 7a and 7b, the vorticity wave structure has a vortex center close to or slightly westward of F4 for the 50 h period band, and hence, the mooring F5 is situated westward of the center, while there is a dipole vortex structure for the 70 h period band, where the strongest vortex center is found east of F4, and a weaker center is found between F4 and F5 (Figures 7c and 7d). Although the cross-shelf dimension (20–40 km) of the unstable baroclinic vorticity waves (Figure 7) is on the order of the mooring spacing (20 km), the rotating signal associated with the waves is expected to be at least partly covered by the moorings as the waves riding on the meandering path of the eastern baroclinic WSC branch shift in and out of the instrument positions.

[22] In a rotating spectrum, a current meter time series obtained on the right hand side (east) of a vortex center should contain more energy in the anticyclonic component, while the cyclonic component should be dominant on the left hand side (west). For the 50 h period band pictured in Figure 7a, Figure 10a confirms that there should be a vortex center somewhere between F4 and F5, where F4 shows up with more anticyclonic rotation and F5 with more cyclonic rotation centered at the 57 h period. The episodes with highest growth rate (Figure 8d) had wave periods around 50–60 h (Figure 8e) and Figure 10a indicates that this oscillation period is a significant signal in the time series (at the 57 h period). For the 70 h period band pictured in Figure 7c, Figure 10b indicates that the F4 and F5 current meters are both to the west of two different vortex centers (at the 73 h period). The phase difference ~180° at the 73 h period

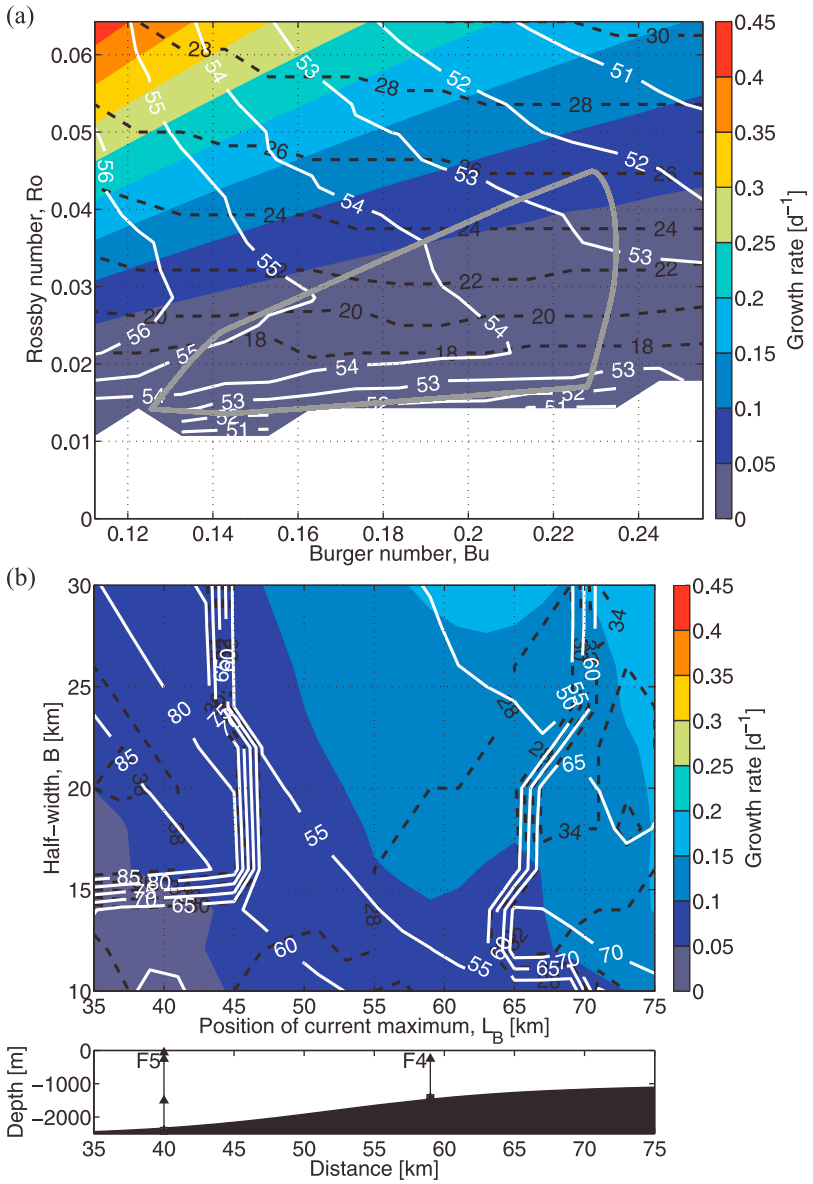

Figure 9. (a) Sensitivity study with variable Rossby and Burger numbers; $\overline{v}_{0,2}$, B, L_B and d are kept constant. The gray curve encompasses the area which the (Ro, Bu) pairs of the unstable periods in Figure 8 falls within. (b) Sensitivity study with variable position (L_B) and half width (B). The other input variables ($\overline{v}_{0,1}$, $\overline{v}_{0,2}$, g', and d) are kept constant. The growth rate of the gravest unstable mode is plotted with colored, solid contours. The corresponding period and wavelength of the gravest unstable mode is displayed with solid white and dotted black contour lines, respectively.

supports the latter interpretation since the two current meters (at F4 and F5) will experience a rotating current vector with a phase lag around 180° in a dipole structure like the one in Figure 7c.

[23] To determine how signal characteristics at specific frequencies change throughout the duration of the time series, complex demodulation [e.g., *Emery and Thomson*, 1998] is used. This method determines the amplitude, phase and thus the ellipse orientation of the cyclonic and anticyclonic rotating component of the velocity time series. The complex demodulation uses least square function fitting, which seeks to determine an optimal function as a linear combination of any specified basis functions for each measuring point, such that the quadratic difference between the estimated value and the observed value is minimized [e.g., *Press et al.*, 1992]. Here, the least square function fitting was solved by use of Singular Value Decomposition (SVD) [e.g., *Press et al.*, 1992]. The demodulated signal was found and tested for sequential segments of different lengths. In order to produce a time series that resolves the $P = 50$ h and $P = 70$ h band for further analysis, a 580 h window function was run over the current data with 10 h separation (or 570 h overlap). Several periods around $P = 50$ h were tested and the $P = 57$ h period oscillation was finally recognized as the strongest signal. A measure of the reliability of this signal tracing method is given by a high amplitude in Figures 11a and 11b together

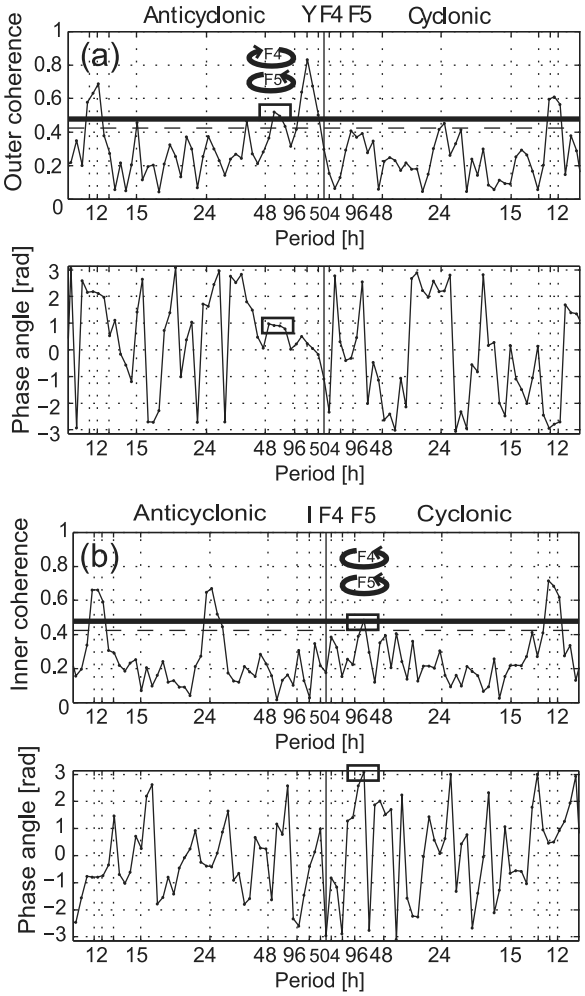

Figure 10. Coherence spectra representing current meter time series from the 2008–2009 observational period. (a) Outer and (b) inner coherence spectrum between current meters at F4 and F5 at 250 m depth. Oscillation periods of particular interest are highlighted by rectangles. Rotational tendencies for the different time series are indicated by rotating arrows. See text for further details. The thick and dashed lines indicate the 95% and 90% confidence levels, respectively.

with a flat phase curve in Figures 11c and 11d over two to three cycles of the period given in Figure 11. Hence, Figure 11 indicates that the strongest/least noisy signal is found between December 2008 and March 2009 for both rotating components with relatively high amplitude and a flat phase curve at $P = 57$ h.

[24] The time periods highlighted by circles in Figure 11a show the events leading to the significant coherence signal in Figure 10a. Hence, an anticyclonic rotating current vector at F4 corresponds to a cyclonic rotating vector at F5 with a rotating period of 57 h. The upper panel in Figure 11a shows that the vortex center has to be to the east of F5 since the anticyclonic signal is weak at F5. It is more unclear where the vortex center is situated relative to F4. When rotating current vectors are recorded within a vortex center, both rotating components will show up in a complex demodulation analysis, and since there is also a strong cyclonic signal at F4, it is likely that F4 is located within the vortex center for most of the time. From the coherence analysis in Figure 10a, one can conclude that the most robust coherent signal is linked to the anticyclonic rotation at F4 and cyclonic rotation at F5, in correspondence with Figure 7a.

4. Discussion

[25] The two-layer model reveals the characteristics of unstable wave modes in the baroclinic eastern WSC branch. Two bands of unstable modes stand out with higher growth rate and exist over a broader range of wavelengths than the others. The primary mode is on the average growing twice as fast as the secondary mode, and has its vortex center close to the position of the maximum current (where the vertical shear is strongest, see Figures 7a and 7b). The secondary mode has an asymmetrical dipole vortex structure, with one center on either flank of the Gaussian baroclinic jet, the strongest pole being on the onshore side (Figures 7c and 7d). The seasonal variation in the strength of the baroclinic instability process is striking (Figure 8d), with a clear maximum in winter time. This is related to the variation in current speed in the upper layer, possibly forced by winter cyclones. During the time intervals when the baroclinic instability process is active, there is a concurrent enhancement of wavelet power in the long periodic range of the spectrum (Figure 5). High amplitudes are also observed in the complex demodulated signal for the wave periods predicted by the linear two-layer model (Figures 8e and 11).

[26] In Figure 12a and 12b, the gradient in the modeled background potential vorticity (PV) is plotted for both layers ($\mathrm{PV} = (f + \frac{\mathrm{d}\overline{v}_n}{\mathrm{d}x})/\overline{h}_n$ within layer n, where $\overline{h}_n$ is the unperturbed layer thickness). A necessary condition for baroclinic instability in a two-layer model is that the gradient in PV changes sign, either within a layer or across the two layers [*Mysak*, 1980]. PV in the lower layer is greatly influenced by the topography, making the gradient negative all the time. In the upper layer, the gradient in PV becomes positive when $\overline{v}_{0,1} > \overline{v}_{0,2}$. In Figure 12c, the intervals when the instability condition is met, are colored green. Intervals with uniform sign of the PV gradient are colored blue. All the episodes with significant growth rate occur within the intervals with changing sign in PV gradient. With the stronger current in the lower layer, the topography inhibits instability. This shows that the intensity of the baroclinic instability process can vary considerably throughout the year, depending mainly on the strength of the northward flow. Based on pressure gauge data, *Morison* [1991] showed that variations in the barotropic component of the WSC are correlated with the seasonal cycle in the wind stress curl in the northern Greenland Sea. *Jónsson et al.* [1992] demonstrated that the observed eddy kinetic energy field in the central and eastern Fram Strait is correlated with the wind power in the Greenland Sea on a seasonal scale, with a time lag of a few months. This does not rule out baroclinic instability as a source of variability on shorter time scales, on the contrary, the wind forcing may sharpen the vertical current shear, leading to unstable conditions. *Benilov* [2001] showed that the influence of topography weakens as the upper layer becomes more detached from the topography (i.e., a thicker lower layer "shields" the upper layer from the topography). In the case when the isopycnal and topographic slope are of the same

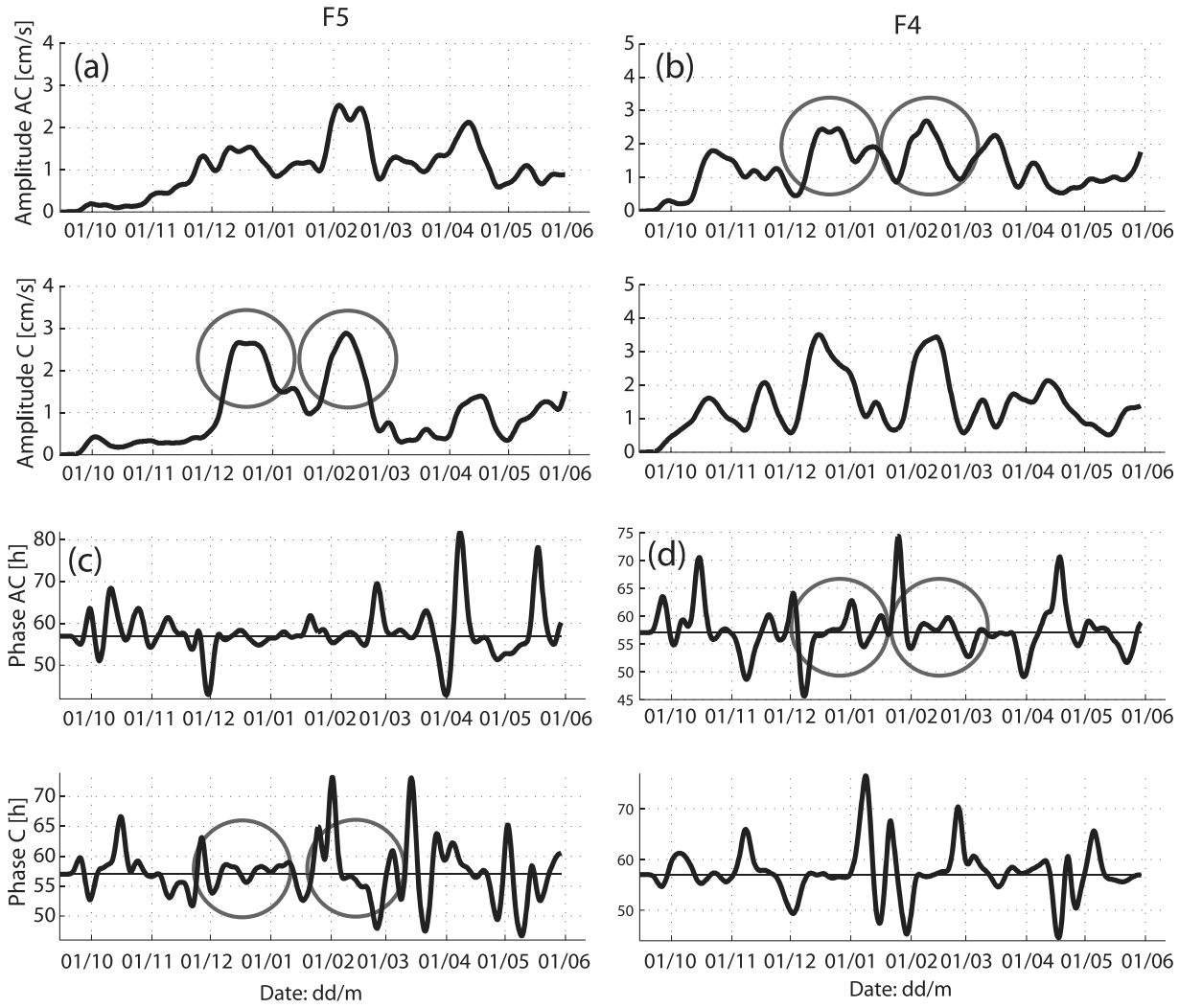

Figure 11. Complex demodulation of current meter data (250 m level, 2008–2009) at (a and c) F5 and (b and d) F4 into (bottom) cyclonic and (top) anticyclonic rotating components, where amplitude (Figures 11a and 11b) and (Figures 11c and 11d) the phase change for the 57 h wave period are shown. The phase change has been converted to wave period by $T_{new} = 2\pi/(\omega_{57h} - d(\text{phase})/dt)$. Events of particular interest during the 2008–2009 current meter time series are highlighted by circles.

sign, the bottom slope can weaken or even eliminate the instability [*Orlanski*, 1969]. This is the case when $\overline{v}_{0,2} > \overline{v}_{0,1}$.

[27] Hovmöller diagrams of northward flow (Figure 13a) and temperature (Figure 13b) spanning the width of the WSC over the continental slope (moorings F0–F6), reveal several episodes of westward propagating anomalies. These episodes are most frequent during winter time, when the baroclinic instability process is most active. The westward propagation is especially evident in temperature (Figure 13b), which serves as a tracer for this process. Similar features were also noted by *Schauer et al.* [2004], who attributed them to eddy-like structures. Coherent eddies spawning off the WSC, propagating westward in the Fram Strait have been reported in many studies [*Johannessen et al.*, 1983; *Johannessen et al.*, 1987; *Gascard et al.*, 1988, 1995], suggesting that a large portion of the recirculating Atlantic water is actually composed of eddies. The present study shows that unstable baroclinic vorticity waves are likely to be encountered in the eastern baroclinic WSC branch, if allowed to grow in amplitude they constitute a generation mechanism for the recirculating eddies in Fram Strait.

4.1. Heat Loss Estimates

[28] In thermal wind balance, geostrophy (equations (1) and (2)) and hydrostaticity combine to maintain a flow in equilibrium. Because a reduction in slope of density surfaces by spreading of the lighter fluid above the heavier fluid would lower the center of gravity and thus the potential energy, the thermal wind equilibrium is not that of least energy. Simultaneously, a slope reduction would also reduce the pressure gradients, the associated geostrophic flow and the kinetic energy of the system, and hence, the state of rest is that of least energy. Since our flow is a vertical shear flow, the thermal wind balance is intrinsically unstable to perturbations (3). The instability process depends crucially on a phase shift with height and is therefore termed baroclinic instability [*Pedlosky*, 1964; *Mysak et al.*, 1981a]. A baroclinic unstable flow will seek a level of lower energy by

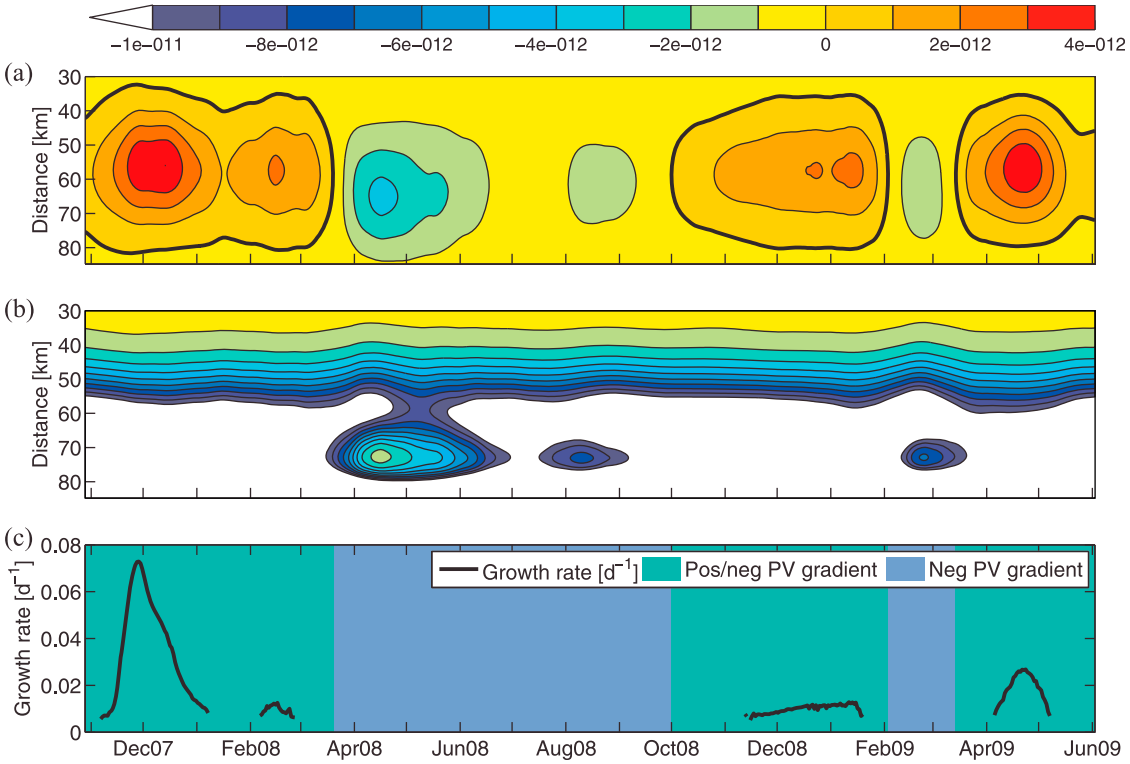

Figure 12. The gradient in background potential vorticity in the (a) upper layer and (b) lower layer. The zero contour is shown with a thicker black line. (c) Time intervals where the potential vorticity gradient is both positive and negative in the domain are indicated with green, while intervals when the potential vorticity gradient is uniformly negative are indicated with blue. The growth rate of the primary unstable mode is also plotted.

relaxation of the density surface in Figure 1 toward static stability [*Gill et al.*, 1974; *Cushman-Roisin and Beckers*, 2011]. In this case (Figure 1), where the lighter and warmer AW is residing above the heavier and cooler LAIW, relaxations imply a westward flow of warm water and an eastward flow of cold water toward the shelf break. In other words, we expect a net offshore heat flux since the temperature increases toward the shelf break (Figure 13b).

[29] Here, we discuss the heat flux in a cross section, since our mooring data and model is set across the WSSl, and use this to estimate the heat loss of the poleward flowing AW along the WSSl. The heat flux in the x direction (across shelf) per unit length of the y direction (along shelf) is defined as

$$q = \rho_0 C_0 \int_{-h(x)}^{\eta_1} uT dz, \tag{8}$$

where ρ_0 is sea water density and $C_0 = 4186$ J kgK^{-1} is the specific heat of sea water. In the two-layer representation of Figure 1, vertical integration gives

$$q = \rho_0 C_0 [u_1 T_1 (H_1 - \eta_1 - \eta_2) + u_2 T_2 (H_2 + \eta_2)]. \tag{9}$$

Here, H_1 and H_2 are the undisturbed thicknesses of the two layers. We now assume vortex generation, and thus perturbing (9), the variables are decomposed into large-scale components denoted by an overbar and vortex components denoted by primes by a low-pass projection operator in time or space. In a shear flow, like the baroclinic eastern branch of the WSC (Figure 1), the isopycnals will be perturbed in accordance with (3). Temperature data (Figure 13b) show that there is a positive temperature gradient toward the barotropic core of the WSC at the shelf break (positive x direction), and there should therefore exist temperature perturbations generated by the vortex field, $T = \overline{T} + T'$. The heat flux equation then becomes

$$\begin{aligned}\overline{q} = \rho_0 C_0 \big[& u_1' T_1' (H_1 + \overline{\eta}_1) + u_2' T_2' (H_2 + \overline{\eta}_2) \\ & + u_1' \eta_1' (\overline{T}_1 + T_1') - u_1' \eta_2' (\overline{T}_1 + T_1') + u_2' \eta_2' (\overline{T}_2 + T_2') \big].\end{aligned} \tag{10}$$

Assume baroclinic instability and let (4) represent the gravest unstable mode. Then by averaging the heat flux (10) over the wave period of the unstable wave mode in (4) we arrive at

$$\begin{aligned}\overline{q} = \rho_0 C_0 \Big[& \overline{u_1' \eta_1' T_1'} + \overline{u_1' \eta_1' T_1'} + \overline{u_1' T_1'} (H_1 + \overline{\eta}_1) + \overline{u_2' T_2'} (H_2 + \overline{\eta}_2) \\ & - \overline{u_1' \eta_2'} (\overline{T}_1 - \overline{T}_2) - \overline{u_1' \eta_2' (T_1' - T_2')} \Big],\end{aligned} \tag{11}$$

where the horizontal flux of interface height is equal for both layers, i.e., $\overline{u_1' \eta_2'} = \overline{u_2' \eta_2'}$ [e.g., *Pedlosky*, 1987, p. 549]. Since the surface displacement perturbations are several orders of magnitude smaller than those of the layer interface

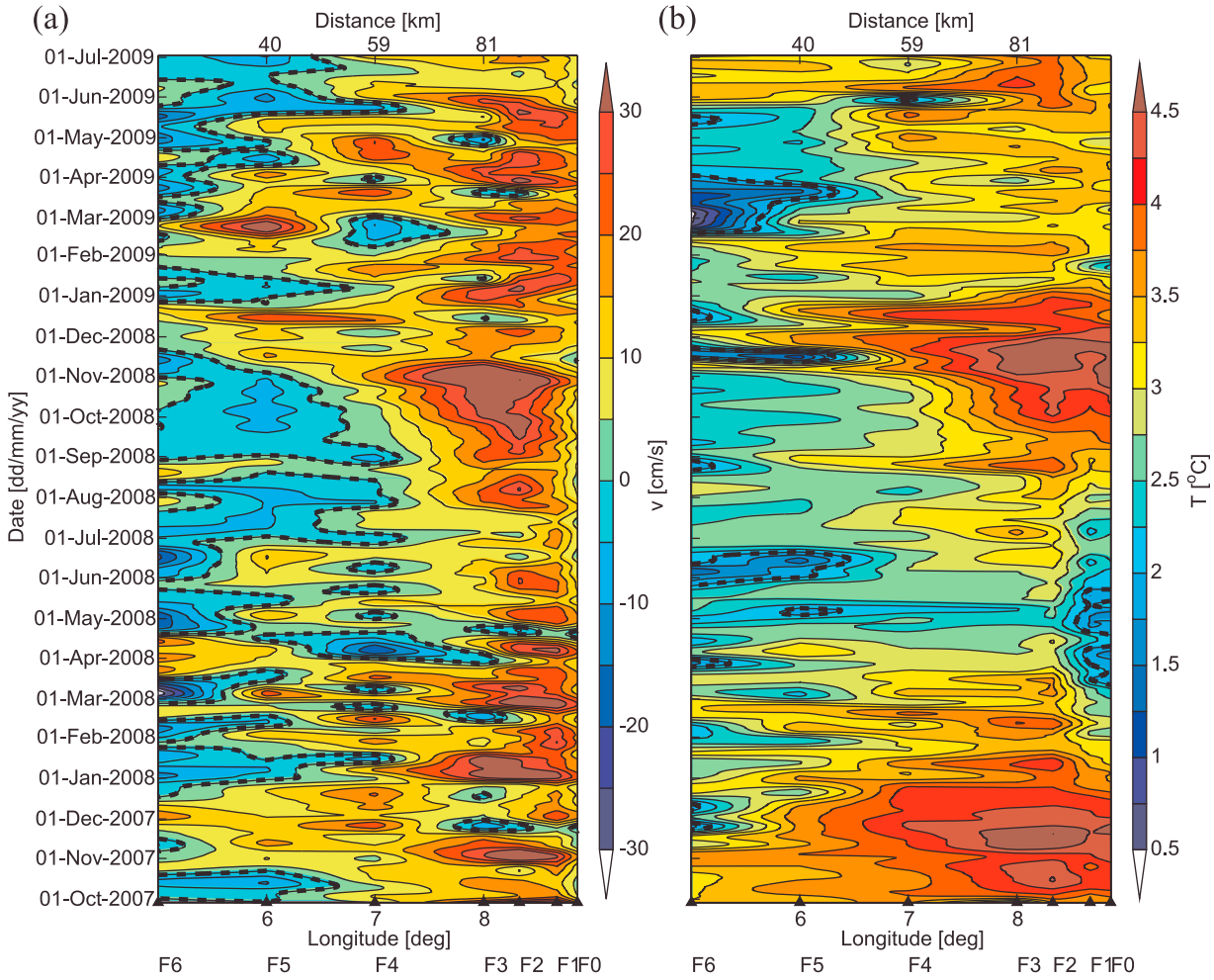

Figure 13. Hovmöller diagram in the 250 m level of moorings F0–F6. (a) Northward flow speed v, the dotted thick contour lines correspond to isolines of zero velocity. (b) Temperature T, the dotted thick contour lines corresponds to 2°C isotherms. All time series are filtered with a 7 day running mean.

$(\eta_2' \gg \eta_1')$, the first two terms on the right hand side in (11) can be neglected, giving

$$\overline{q} = \rho_0 C_0 \Big[\overline{u_1' T_1'}(H_1 + \overline{\eta}_1) + \overline{u_2' T_2'}(H_2 + \overline{\eta}_2) - \overline{u_1' \eta_2'}\big(\overline{T}_1 - \overline{T}_2\big) - \overline{u_1' \eta_2'}\big(T_1' - T_2'\big)\Big]. \quad (12)$$

The across-shelf heat flux equation (12) consists of three different heat loss processes in which a fundamental assumption is that ocean vortices mix tracers along isopycnals and not across them. The first two terms represent the heat flux in each layer when the vortices of the gravest unstable mode work on a background temperature gradient, bringing warm water along isopycnals to a cold region and cold water to a warm region. The last term in (12) is a front-confined mixing term, which can be parameterized as a Fickian diffusion along isopycnals with a diffusion coefficient [*Gent and Mcwilliams*, 1990; *Gent et al.*, 1995]. Here, we assume uniform temperature layers with no horizontal temperature gradients along isopycnals, and hence, the isopycnal mixing terms will vanish in our two-layered model (Figure 1). We are left with the third term in (12)

$$\overline{q} = -\rho_0 C_0 \overline{u_1' \eta_2'}\big(\overline{T_1} - \overline{T_2}\big), \quad (13)$$

which is the vortex-induced transport of temperature [e.g., *Gent et al.*, 1995] when the horizontal density gradients decrease due to conversion or release of available potential energy by the gravest unstable wave mode. Hence, the density front or the geostrophic control is leveling off and allowing warm water to flow westward and cold water to flow eastward, producing a net westward heat flux and a heat loss on the baroclinic eastern branch of the WSC (Figure 1).

[30] In Figure 14, the heat loss associated with the primary mode is plotted, calculated by (13), using the eigenvectors (u_1', η_2') resulting from the two-layer model and the 30 day smoothed temperature record in the 250 m and 1500 m levels as background temperature field $(\overline{T_1}, \overline{T_2})$. The maximum amplitude of the perturbation velocity and interface displacement has been scaled by 40% of the amplitude of the background field, yielding current amplitudes of 4–8 cm s^{-1}.

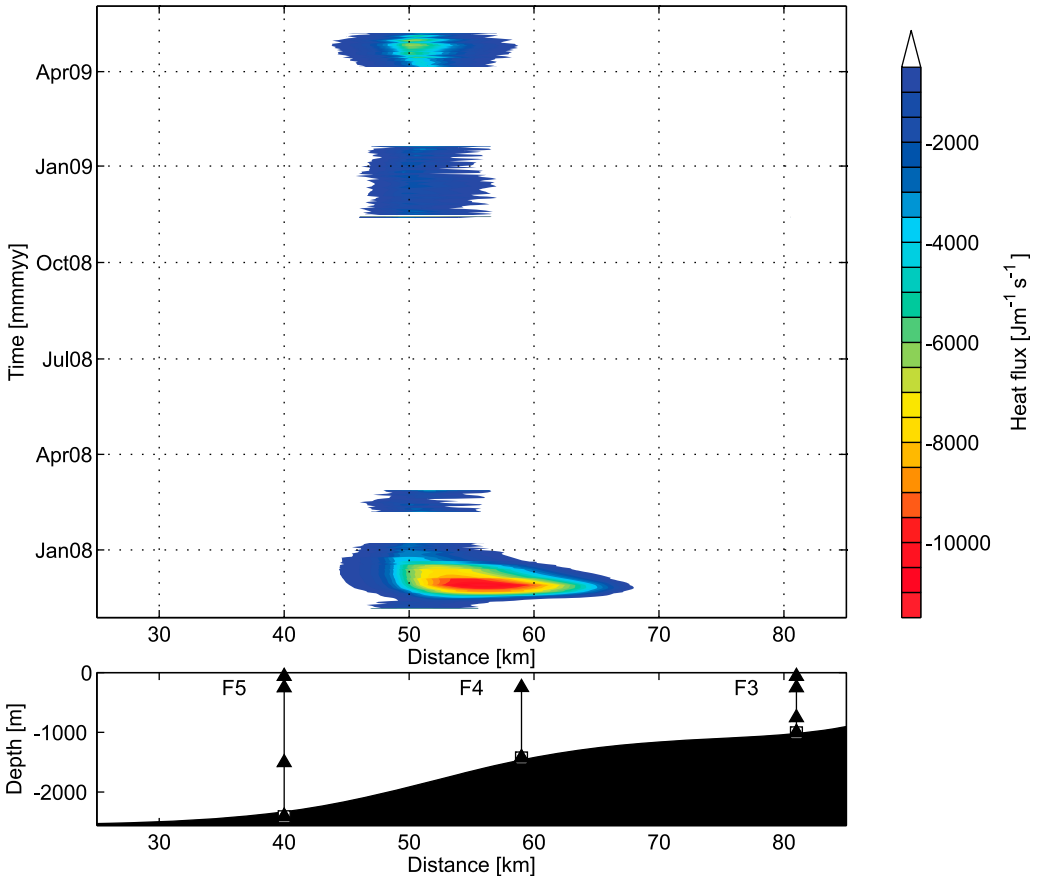

Figure 14. Hovmöller diagram of modeled heat flux in the upper layer (negative values correspond to an offshore heat flux), calculated from equation (13).

The most intense heat loss caused by the primary mode is occurring during the first unstable episode in Figure 8 (late November 2007 to early January 2008), reaching 11800 W m^{-1}. For this episode, the maximum heat loss is taking place just a couple of kilometers west of F4. For the later (and weaker) heat loss events, the maximum is located further offshore (halfway between F4 and F5). The mean heat loss during the unstable episodes is ~3100 W m^{-1}.

[31] Following the ideas of *Helland-Hansen and Nansen* [1912] and *Boyd and D'Asaro* [1994], that lateral exchange with colder surrounding waters is the primary mechanism for cooling of the subsurface warm core of the WSC, we will estimate the contribution to lateral heat loss [*Nilsen et al.*, 2006; *Teigen et al.*, 2010] from the fastest growing unstable wave mode existing in the eastern baroclinic WSC branch. Thus, we assume a temperature perturbation of a background temperature gradient between the warm AW and the colder local water (e.g., LAIW), and calculate the $\rho_0 C_0 \overline{u_1' T_1'}$ vortex heat flux at the 250 m level. We base our estimates on the wave characteristic found in Figures 11a and 11c for the 2008–2009 mooring period, and extract the oscillating temperature signal (P = 57 h) the same way through least square function fitting by using SVD. A time series of the horizontal heat flux [W m^{-2}] at F4 is presented in Figure 15b, based on the rotating wave field in Figures 11a and 11c, and the demodulated temperature signal at the P = 57 h oscillating period. The same procedure is performed on the 2007–2008 mooring data where P = 53 h shows up as the most significant wave period, and heat flux estimates for the 2007–2008 period is given in Figure 15a. Several episodes of westward heat flux (negative sign) can be seen, mostly within 2–4000 W m^{-2}. The most interesting heat loss episode is occurring during the first episode in Figure 8 (late November 2007 to early January 2008) when the growth rate of the primary unstable mode reached its maximum. Figure 15a has a westward maximum around 3000 W m^{-2} during the same time period. A singular event of westward heat flux peaking at 10000 W m^{-2} occurs in December 2008 (Figure 15b), also concurring with the growth rate time series in Figure 8d.

[32] The vertical shear in the baroclinic eastern branch of the WSC represents a geostrophic control on the westward heat flux. The western flank of the current branch is located at the transition from the WSSl into the abyssal interior (the "flat" bottom portion) of Fram Strait. Episodes of intense baroclinic instability will break down the control and eddy-induced transport of temperature (12) will create a westward heat flux (when $\overline{v}_1 > \overline{v}_2$), resulting in a heat loss in the poleward flowing AW of the WSC. The heat budget for the interior (flat bottom portion) of the eastern Fram Strait may be written as

$$Q = Y\,\overline{q} = YW\,\overline{Q_s}, \tag{14}$$

where $\overline{q}$ is the east-west heat flux per unit length in the y direction, $Y \sim 400$ km is the along-shelf dimension of our

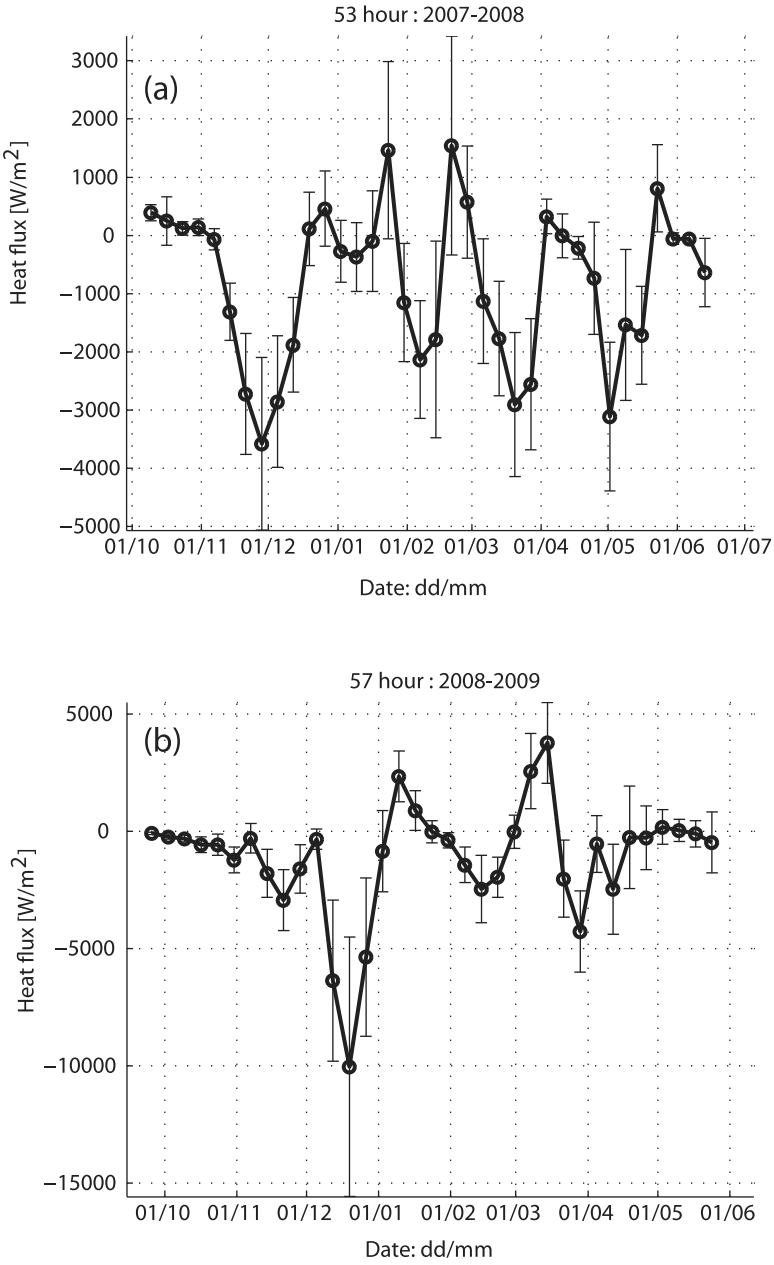

Figure 15. A time series of the horizontal heat flux (W m^{-2}) at F4 based on the wave signal P = 57 h at the 250 m level: (a) deployment year 2007–2008 and (b) deployment year 2008–2009.

study area, assuming the slope profile (5) to be valid along the whole WSS, W is the width of the interior, and $\overline{Q_s}$ is the averaged surface heat flux over the interior surface area YW. This heat balance assumes that the net heat exchange with the atmosphere in the interior is balanced by lateral eddy fluxes originating at the western perimeter of the WSC. The heat loss Q in TW (1 $TW = 1 \times 10^{12}$) can be estimated through calculation of the surface heat flux in our study area, but also by means of (12). We are able to estimate the terms in (12) from a combination of our data and the linear model. Multiplying the time series in Figure 15 by the upper layer thickness gives the first term in (12), while the third term is given by Figure 14. Assuming small velocity and temperature perturbations in the lower layer, and no isopycnal diffusion of temperature at the interface, the former two terms will determine the lateral isopycnal vortex heat flux in (12). Using an upper layer thickness of 800 m in the vorticity wave heat flux ($\overline{q_1}$, term 1 in (12)), it is evident that this term will be larger than the vortex induced transport of temperature ($\overline{q_3}$, term 3 in (12)) associated with the leveling of the interface front between the two layers. If W is set to 10 km and $\overline{q_1}$ = 3000 W m^{-2} × 800 m = 2.4 MW m^{-1}, term 1 will contribute to $\overline{Q_s}$ by 240 W m^{-2}, while the most intense heat loss by term 3 (late November 2007) results in a 1.8 W m^{-2} contribution to $\overline{Q_s}$.

[33] Important conclusions can be drawn from these estimates. First, the overall $\overline{Q_s}$ has the same order of magnitude as the winter surface heat loss estimates of, e.g., *Saloranta and*

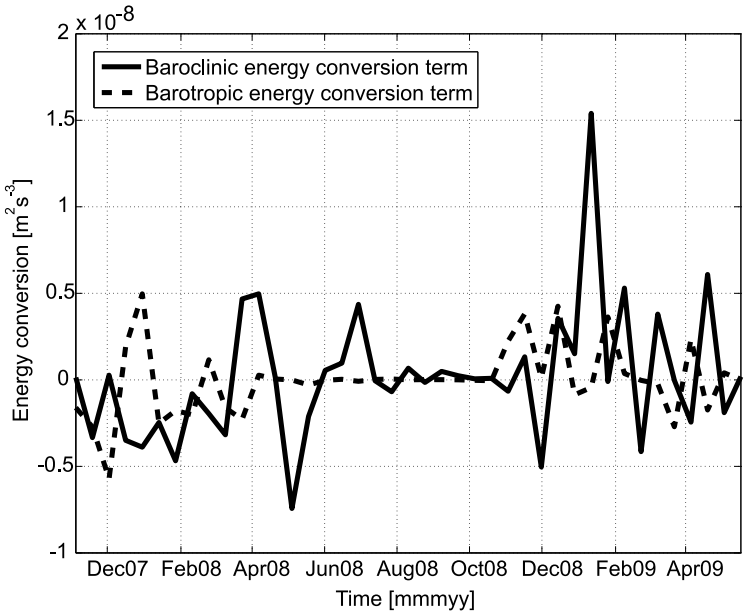

Figure 16. Baroclinic and barotropic energy conversion terms.

Haugan [2004]. Secondly, even though the $\overline{q_3}$ contribution is small, there can be no westward heat flux unless the geostrophic control is reduced through baroclinic instability as signified by η_2'. Hence, $\overline{q_3}$ represents the reduction in the westward heat flux blocking, while $\overline{q_1}$ represents the actual heat loss based on the characteristics of the unstable vorticity wave and the background temperature gradient.

4.2. Comparison With Earlier Results

[34] Further south, in the Norwegian Atlantic Current at 63°N, *Mysak and Schott* [1977] observed that the current showed fluctuations with periods 48–72 h. Applying an analytical two-layer model of baroclinic instability, they found that the most unstable mode peaked at P = 60 h. Using the same model as *Mysak and Schott* [1977], *Hanzlick* [1983] also studied baroclinic instability in the WSC, finding periods of 72–96 h, with wavelengths 30–40 km. This is in the upper end of the period range detected by our analysis, which lies closer to the numbers of *Mysak and Schott* [1977]. *Hanzlick* [1983] presented two calculation cases, in the case resembling the eastern baroclinic WSC branch he used a much shallower upper layer thickness (250 m) and thicker lower layer (2000 m) than in the present analysis, which might explain some of the differences. The growth rate of the baroclinic instabilities in the WSC is weaker than in the Norwegian Atlantic Current, which is related to the much steeper slope outside Svalbard (6×10^{-2} as opposed to 1×10^{-2} used in the analysis by *Mysak and Schott* [1977]). According to observations by *Schott and Bock* [1980], barotropic instability can feed energy back into the mean field at a larger rate than the baroclinic instability process is able to extract it. The baroclinic conversion from the mean flow to eddy energy is given by *Spall et al.* [2008]

$$BC = -\frac{g}{\rho_0}\frac{\mathrm{d}\overline{\eta}_2}{\mathrm{d}x}\overline{u_1'\sigma_{\theta,1}'}, \tag{15}$$

where $\overline{u_1'\sigma_{\theta,1}'}$ is the across-slope eddy density flux. The barotropic conversion term is given by

$$BT = \overline{u_1'v_1'}\frac{\mathrm{d}\overline{u}_1}{\mathrm{d}x}, \tag{16}$$

where $\overline{u_1'v_1'}$ is the eddy momentum flux. For our purposes, the background terms ($\frac{\mathrm{d}\overline{\eta}_2}{\mathrm{d}x}$ and $\frac{\mathrm{d}\overline{u}_1}{\mathrm{d}x}$) were based on the time series of the modeled baroclinic Gaussian jet profile (6) and the resulting interface displacement (Figure 4). The eddy fluxes were calculated for the 250 m level of mooring F4. As there was no measurements of salinity at this level, the density was calculated from temperature, using a polynomial fit between temperature and density in the 250 m level at F3, where both temperature and salinity were measured (similar to the procedure by *Schott and Bock* [1980]). In order to focus on the period band which the baroclinic vorticity waves are expected to occupy, based on the analysis in section 3.2, the time series was then band-pass filtered between 35 and 75 h. Then the time series was split in 14 day intervals, extracting the fluctuating component. In Figure 16, baroclinic and barotropic energy conversion terms are plotted. Although crude, the calculations of the baroclinic and barotropic conversion can give us an idea of the level of conversion where the interface is sloping the most. BC and BT are on the same order of magnitude, but the baroclinic conversion is exceeding the barotropic on several occasions. During the summer and autumn months of 2008 (July–October), both baroclinic and barotropic energy conversion are very quiet. The first major unstable event (late November 2007 to early January 2008) coincides with a time interval of negative (energy being extracted from the background field) baroclinic conversion.

[35] *Teigen et al.* [2010] considered barotropic instability in the eastern barotropic WSC branch. The strong horizontal shear on the shoreward flank of the asymmetric current profile found by *Teigen et al.* [2010] resulted in mean and

peak growth rates up to 10 times those found in the baroclinic eastern WSC branch. The vorticity wave in the barotropic case was located at the shelf break, while in the baroclinic branch the vorticity wave associated with the primary mode is positioned close to the current maximum. This yields different modus operandi for the barotropic and the baroclinic vorticity waves; the barotropic mode enhancing isopycnal eddy diffusion of heat from the eastern barotropic WSC branch to the shelf waters, while the baroclinic mode is eroding the geostrophic control on the eastern baroclinic WSC branch (13) and at the same time significantly contributing to offshore heat loss (14) through westward isopycnal eddy diffusion.

5. Conclusions

[36] The present analysis indicates that the eastern baroclinic branch of the WSC is susceptible to baroclinic instability. Characteristic wavelengths of the resulting unstable vorticity waves are 15–30 km, with associated wave periods of 35–75 h. Wavelet and rotating vector analysis detected significant energy at similar periods and time intervals as the stability analysis showed, especially around 53–57 h wave periods. The resulting modal structure represents a mechanism for unlocking the geostrophic control on the eastern baroclinic WSC branch, setting the scene for offshore heat loss by isopycnal eddy diffusion. By complex demodulation of the temperature and current data, the signal associated with the 53–57 h mode has been studied in detail. Several episodes of intense offshore heat flux were identified, reaching values of ~240 W m^{-2}, which is comparable with the winter heat loss from the surface layer of the WSC reported in earlier studies.

[37] **Acknowledgments.** The present study was supported by the Norwegian Research Council through its International Polar Year programme and the project iAOOS-Norway: Closing the Loop (grant 176096/S30, http://www.iaoos.no/). We would like to acknowledge U. Schauer and E. Fahrbach at the Alfred Wegener Institute (AWI) for their persistent effort to continue the mooring programme in the eastern Fram Strait. In preparing the wavelet plots, we have used MATLAB routines developed by A. Grinsted. The routines are available at http://www.pol.ac.uk/home/research/waveletcoherence/. A plotting routine for progressive vector diagrams has been adapted from J. M. Lilly (http://www.jmlilly.net/).

References

Aagaard, K., and P. Greisman (1975), Toward new mass and heat budgets of the Arctic Ocean, *J. Geophys. Res.*, *80*, 3821–3827.

Aagaard, K., J. H. Swift, and E. C. Carmack (1985), Thermohaline circulation in the Arctic Mediterranean seas, *J. Geophys. Res.*, *90*, 4833–4846.

Benilov, E. S. (2001), Baroclinic instability of two-layer flows over one-dimensional bottom topography, *J. Phys. Oceanogr.*, *31*, 2019–2025, doi:10.1175/1520-0485(2001)031<2019:BIOTLF>2.0.CO;2.

Bourke, R. H., and A. M. W. R. G. Paquette (1988), The westward turning branch of the West Spitsbergen Current, *J. Geophys. Res.*, *93*, 14,065–14,077.

Boyd, T. J., and E. A. D'Asaro (1994), Cooling of the West Spitsbergen Current: Wintertime observations west of Svalbard, *J. Geophys. Res.*, *99*, 22,597–22,618.

Cokelet, E. D., N. Tervalon, and J. G. Bellingham (2008), Hydrography of the West Spitsbergen Current, Svalbard branch: Autumn 2001, *J. Geophys. Res.*, *113*, C01006, doi:10.1029/2007JC004150.

Cushman-Roisin, B., and J.-M. Beckers (2011), *Introduction to Geophysical Fluid Dynamics*, Academic, in press.

Davies, A. M., J. Xing, and B. Gjevik (2003), Barotropic eddy generation by flow instability at the shelf edge: Sensitivity to open boundary conditions, inflow and diffusion, *J. Geophys. Res.*, *108*(C2), 3035, doi:10.1029/2001JC001137.

Dmitrenko, I. A., I. V. Polyakov, S. A. Kirillov, L. A. Timokhov, I. E. Frolov, V. T. Sokolov, H. L. Simmons, V. V. Ivanov, and D. Walsh (2008), Toward a warmer Arctic Ocean: Spreading of the early 21st century Atlantic Water warm anomaly along the Eurasian Basin margins, *J. Geophys. Res.*, *113*, C05023, doi:10.1029/2007JC004158.

Eldevik, T., J. E. Ø. Nilsen, D. Iovino, K. A. Olsson, A. B. Sandø, and H. Drange (2009), Observed sources and variability of Nordic seas overflow, *Nat. Geosci.*, *2*, 406–410, doi:10.1038/ngeo518.

Emery, W. J., and R. E. Thomson (Eds.) (1998), *Data Analysis Methods in Physical Oceanography*, Elsevier, Kidlington, U. K.

Fahrbach, E., G. Rohardt, U. Schauer, J. Meincke, S. Østerhus, and J. Verduin (2003), Direct measurements of heat and mass transports through Fram Strait, *ICES Mar. Sci. Symp.*, *291*, 378–381.

Fer, I., R. Skogseth, and F. Geyer (2010), Internal waves and mixing in the marginal ice zone near the Yermak Plateau, *J. Phys. Oceanogr.*, *40*, 1613–1630, doi:10.1175/2010JPO4371.1.

Gascard, J.-C., C. Kergomard, P.-F. Jeannin, and M. Fily (1988), Diagnostic study of the Fram Strait marginal ice zone during summer from 1983 and 1984 Marginal Ice Zone Experiment Lagrangian observations, *J. Geophys. Res.*, *93*, 3613–3641.

Gascard, J.-C., C. Richez, and C. Rouault (1995), New insights on large-scale oceanography in Fram Strait: The West Spitsbergen Current, *Cont. Shelf Res.*, *49*, 131–182.

Gent, P. R., and J. C. Mcwilliams (1990), Isopycnal mixing in ocean circulation models, *J. Phys. Oceanogr.*, *20*, 150–155, doi:10.1175/1520-0485(1990)020<0150:IMIOCM>2.0.CO;2.

Gent, P. R., J. Willebrand, T. J. McDougall, and J. C. McWilliams (1995), Parameterizing eddy-induced tracer transport in Ocean Circulation Models, *J. Phys. Oceanogr.*, *25*, 463–474, doi:10.1175/1520-0485(1995)025<0463:PEITTI>2.0.CO;2.

Gill, A., J. Green, and A. Simmons (1974), Energy partition in the large-scale ocean circulation and the production of mid-ocean eddies, *Deep Sea Res.*, *21*, 499–528, doi:10.1016/0011-7471(74)90010-2.

Gjevik, B. (2002), *Unstable and Neutrally Stable Modes in Barotropic and Baroclinic Shelf Slope Currents*, *Prepr. Ser.*, vol. 1, Dep. of Math., Univ. of Oslo, Oslo, Norway.

Hanzlick, D. J. (1983), The West Spitzbergen Current: Transport, forcing and variability, Ph.D. thesis, Univ. of Wash., Seattle, Wash.

Helland-Hansen, B., and F. Nansen (1912), The sea west of Spitsbergen, *Videnskapsselsk. Skr. I*, *12*, 1–89.

Jakobsson, M., R. Macnab, L. Mayer, R. Anderson, M. Edwards, J. Hatzky, H. W. Schenke, and P. Johnson (2008), An improved bathymetric portrayal of the Arctic Ocean: Implications for ocean modeling and geological, geophysical and oceanographic analyses, *Geophys. Res. Lett.*, *35*, L07602, doi:10.1029/2008GL033520.

Johannessen, J. A., et al. (1987), Mesoscale eddies in the Fram Strait marginal ice zone during the 1983 and 1984 Marginal Ice Zone Experiments, *J. Geophys. Res.*, *92*, 6754–6772.

Johannessen, O. M., J. A. Johannessen, J. Morison, B. A. Farrelly, and E. A. S. Svendsen (1983), Oceanographic conditions in the marginal ice zone north of Svalbard in early fall 1979 with an emphasis on mesoscale processes, *J. Geophys. Res.*, *88*, 2755–2769.

Jónsson, S., A. Foldvik, and K. Aagaard (1992), The structure and atmospheric forcing of the mesoscale velocity field in Fram Strait, *J. Geophys. Res.*, *97*, 12,585–12,600, doi:10.1029/2002JC001554.

Kasajima, Y., and H. Svendsen (2002), Tidal features in the Fram Strait, *Cont. Shelf Res.*, *22*, 2461–2477, doi:10.1016/S0278-4343(02)00132-2.

Kawabe, M. (1982), Coastal trapped waves in a two-layer ocean: Wave properties when the density interface intersects a sloping bottom, *J. Oceanogr. Soc. Jpn.*, *38*, 115–124.

Liu, Y., X. San Liang, and R. H. Weisberg (2007), Rectification of the bias in the wavelet power spectrum, *J. Atmos. Oceanic Technol.*, *24*, 2093–2102, doi:10.1175/2007JTECHO511.1.

Livingstone, D., and T. C. Royer (1980), Eddy propagation determined from rotary spectra, *Deep Sea Res. Part A*, *27*, 823–835.

Manley, T. (1995), Branching of Atlantic Water within the Greenland-Spitsbergen Passage: An estimate of recirculation, *J. Geophys. Res.*, *100*, 20,627–20,634.

Morison, J. (1991), Seasonal variations in the West Spitsbergen Current estimated from bottom pressure measurements, *J. Geophys. Res.*, *96*, 18,381–18,395.

Mysak, L. A. (1980), Recent advances in shelf wave dynamics, *Rev. Geophys.*, *18*, 211–241.

Mysak, L. A., and F. Schott (1977), Evidence for baroclinic instability of the Norwegian Current, *J. Geophys. Res.*, *82*, 2087–2095.

Mysak, L. A., R. D. Muench, and J. D. Schumacher (1981a), Baroclinic instability in a downstream varying channel: Shelikof Strait, Alaska, *J. Phys. Oceanogr.*, *11*, 950–969, doi:10.1175/1520-0485(1981)011<0950:BIIADV>2.0.CO;2.

Mysak, L. A., E. R. Johnson, and W. W. Hsieh (1981b), Baroclinic and barotropic instabilities of coastal currents, *J. Phys. Oceanogr.*, *11*, 209–230, doi:10.1175/1520-0485(1981)011<0209:BABIOC>2.0.CO;2.

Nilsen, F., B. Gjevik, and U. Schauer (2006), Cooling of the West Spitsbergen Current: Isopycnal diffusion by topographic vorticity waves, *J. Geophys. Res.*, *111*, C08012, doi:10.1029/2005JC002991.

Orlanski, I. (1969), The influence of bottom topography on the stability of jets in a baroclinic fluid, *J. Atmos. Sci.*, *26*, 1216–1232, doi:10.1175/1520-0469(1969)026<1216:TIOBTO>2.0.CO;2.

Orvik, K. A., and P. Niiler (2002), Major pathways of Atlantic Water in the northern North Atlantic and Nordic Seas toward Arctic, *Geophys. Res. Lett.*, *29*(19), 1896, doi:10.1029/2002GL015002.

Pedlosky, J. (1964), The stability of currents in the atmosphere and the ocean: Part I, *J. Atmos. Sci.*, *21*, 201–219, doi:10.1175/1520-0469(1964)021<0201:TSOCIT>2.0.CO;2.

Pedlosky, J. (1987), *Geophysical Fluid Dynamics*, 2nd ed., 320 pp., Springer, New York.

Press, W. H., S. A. Teukolsky, W. T. Vetterling, and B. P. Flannery (1992), *Numerical recipes in Fortran* 77*: The art of scientific computing*, vol. 1, 2nd ed., Cambridge Univ. Press, Cambridge, U. K.

Saloranta, T. M., and P. M. Haugan (2001), Interannual variability in the hydrography of Atlantic Water northwest of Svalbard, *J. Geophys. Res.*, *106*, 13,931–13,943.

Saloranta, T. M., and P. M. Haugan (2004), Northward cooling and freshening of the warm core of the West Spitsbergen Current, *Polar Res.*, *23*, 79–88.

Schauer, U., E. Fahrbach, S. Østerhus, and G. Rohardt (2004), Arctic warming through the Fram Strait: Oceanic heat transport from 3 years of measurements, *J. Geophys. Res.*, *109*, C06026, doi:10.1029/2003JC001823.

Schauer, U., A. Beszczynska-Möller, W. Walczowski, E. Fahrbach, J. Piechura, and E. Hansen (2008), Variation of measured heat flow through the Fram Strait between 1997 and 2006, in *Arctic-Subarctic Ocean Fluxes*, edited by R. R. Dickson, J. Meincke, and P. Rhines, pp. 65–85, Springer, New York.

Schott, F., and M. Bock (1980), Determination of energy interaction terms and horizontal wavelengths for low frequency fluctuations in the Norwegian Current, *J. Geophys. Res.*, *87*, 4007–4014.

Sirevaag, A., and I. Fer (2009), Early spring oceanic heat fluxes and mixing observed from drift stations north of Svalbard, *J. Phys. Oceanogr.*, *39*, 3049–3069, doi:10.1175/2009JPO4172.1.

Spall, M. A., R. S. Pickart, P. S. Fratantoni, and A. J. Plueddemann (2008), Western Arctic shelfbreak eddies: Formation and transport, *J. Phys. Oceanogr.*, *38*, 1644–1668, doi:10.1175/2007JPO3829.1.

Steele, M., and T. Boyd (1998), Retreat of the cold halocline layer in the Arctic Ocean, *J. Geophys. Res.*, *103*, 10,419–10,435.

Steele, M., and J. Morison (1993), Hydrography and vertical fluxes of heat and salt northeast of Svalbard in autumn, *J. Geophys. Res.*, *98*, 10,013–10,024.

Teigen, S. H. (2011), A two-layer model for linear stability analysis of shelf-slope currents, *Rep. Meteorol. Oceanogr. 1*, Geophys. Inst., Univ. of Bergen, Bergen, Norway.

Teigen, S. H., F. Nilsen, and B. Gjevik (2010), Barotropic instability in the West Spitsbergen Current, *J. Geophys. Res.*, *115*, C07016, doi:10.1029/2009JC005996.

Torrence, C., and G. P. Compo (1998), A practical guide to wavelets, *Bull. Am. Meteorol. Soc.*, *79*, 61–78.

Turner, J. S. (2010), The melting of ice in the Arctic Ocean: The influence of double-diffusive transport of heat from below, *J. Phys. Oceanogr.*, *40*, 249–256, doi:10.1175/2009JPO4279.1.

Walczowski, W., and J. Piechura (2007), Pathways of the Greenland Sea warming, *Geophys. Res. Lett.*, *34*, L10608, doi:10.1029/2007GL029974.

Walczowski, W., J. Piechura, R. Osinski, and P. Wieczorek (2005), The West Spitsbergen Current volume and heat transport from synoptic observations in summer, *Deep Sea Res.*, *52*, 1374–1391, doi:10.1016/j.dsr.2005.03.009.

A. Beszczynska-Möller, Alfred Wegener Institute for Polar and Marine Research, Köperstr. 8, D-27570 Bremerhaven, Germany.

B. Gjevik, Department of Mathematics, University of Oslo, PO Box 1032, Blindern, N-0315 Oslo, Norway.

F. Nilsen, R. Skogseth, and S. H. Teigen, Department of Arctic Geophysics, University Centre in Svalbard, PO Box 156, N-9170 Longyearbyen, Norway. (sigurd.henrik.teigen@unis.no)